Clim Dyn
DOI 10.1007/s00382-009-0703-8

Upper-ocean heat budget and ocean eddy transport in the south-east Pacific in a high-resolution coupled model

Thomas Toniazzo · Carlos R. Mechoso · Leonard C. Shaffrey · Julia M. Slingo

Received: 17 March 2009 / Accepted: 30 October 2009

Abstract We present an analysis of the oceanic heat advection and its variability in the upper 500 m in the southeastern tropical Pacific (100W–75W, 25S–10S) as simulated by the global coupled model HiGEM, which has one of the highest resolutions currently used in long-term integrations. The simulated climatology represents a temperature advection field arising from transient small-scale (<450 km) features, with structures and transport that appear consistent with estimates based on available observational data for the mooring at 20S, 85W. The transient structures are very persistent (>4 months), and in specific locations they generate an important contribution to the local upper-ocean heat budget, characterised by scales of a few hundred kilometres, and periods of over a year. The contribution from such structures to the local, long-term oceanic heat budget however can be of either sign, or vanishing, depending on the location; and, although there appears some organisation in preferential areas of activity, the average over the entire region is small. While several different mechanisms may be responsible for the temperature advection by transients, we find that a significant, and possibly dominant, component is associated with vortices embedded in the large-scale, climatological salinity gradient associated with the fresh intrusion of mid-latitude intermediate water which penetrates northwestward beneath the tropical thermocline.

T. Toniazzo (✉) · L. C. Shaffrey · J. M. Slingo
NCAS-Climate, Department of Meteorology,
University of Reading, Reading RG6 6BB, UK
e-mail: t.toniazzo@reading.ac.uk

C. R. Mechoso
UCLA, California, USA

1 Introduction

The eastern parts of the subtropical Pacific and Atlantic Oceans are characterised by coastal upwelling and low sea surface temperatures (SSTs). The equatorward branches of the subtropical anticyclones flow above those cold oceans, where extensive and persistent decks of stratocumulus clouds (Sc) develop. Above the boundary layer and the Sc deck, the tropospheric flow is characterised by large-scale subsidence associated with the descending branches of the tropical Hadley–Walker circulation. The cloud decks reduce the short-wave radiation received at the ocean surface by about 100 W/m^2 (Cronin et al. 2006). These oceanic areas exert a strong influence on the mean climatology of the tropical basins (Mitchell and Wallace 1992) and on the heat budget of the tropical circulation (Hastenrath 1991; Norris and Leovy 1994).

It has been recognised for a long time that the system described in the previous paragraph depends on coupled atmosphere–ocean feedbacks (e.g. Ma et al. 1996; Philander et al. 1996; de Szoeke and Xie 2007; Takahashi and Battisti 2007). Basically, the cool atmospheric planetary boundary-layer (PBL) maintains the Sc; these intercept solar radiation and help, in turn, maintaining the cool SSTs. However, recent studies have stressed a more complex role of the ocean. Accordingly, offshore Ekman transport from regions of coastal upwelling contributes significantly to the cold surface climatology of the coastal waters. In the south-east Pacific (SEP), Colbo and Weller (2007) have shown from ship-based, XBT-line, and buoy data over a period of 4 years, that the net surface heat budget is positive at the location of the IMET buoy (20S, 85W) of the Wood's Hole Oceanographic Institute—i.e., the ocean gains heat in spite of cloud short-wave forcing. This is consistent with reanalysis data from both ERA40

Published online: 19 November 2009

and NCEP. Without cold oceanic advection, oceanic temperatures would increase, and equilibrium would be re-established either by increased heat export (with potential implications for the tropical thermocline), or by warmer SSTs and thus reduced net gain from surface fluxes (with potential implications for the regional PBL coupling and cloud-cover).

Colbo and Weller (2007) also showed that at the specific location of the buoy, mean oceanic advection, i.e. advection implied by time-mean oceanic temperatures and currents, is insufficient to balance the surface heat budget. They suggest that an additional advective cooling of the order of 20 W/m^2 over the water column down to 250 m is provided by transient ocean eddies. This suggestion raises interesting questions concerning the large-scale controls on the climatology of the SEP, the mechanisms that determine it, and its sensitivity to various physical atmospheric and oceanic processes. There is a strong motivation for attempting to address such questions . The SEP is known as a problem area for coupled general-circulation models (GCMs), with significant implications for the simulation of the climate of the entire tropical Pacific (Mechoso et al. 1995; Ma et al. 1996; Large et al. 1997) and its variability (Manganello and Huang 2008; Toniazzo 2009). Without a better understanding of such sensitivities on tropical and subtropical Sc forcing it may not be possible to narrow the main uncertainties that affect global climate projections (Bony and Dufresne 2005), or to achieve a realistic representation of tropical climate variability with GCMs (Toniazzo 2009).

Motivated by the above, the present paper attempts to address the specific need to better understand how much of the upper-ocean variability in the SEP is controlled by surface fluxes; how much is attributable to ocean dynamics; and how this variability rectifies onto the mean climatology. These issues have remained very uncertain. On the one hand, the SEP is one of the areas of the world ocean most lacking in observational data. On the other hand, the extent to which GCMs, and especially coupled climate models, can represent advection associated with oceanic transients is doubtful. The upper-ocean thermal and salinity structure and the surface forcing simulated by most GCMs may not be sufficiently realistic, and one does expect some sensitivity to the model's resolution. Oceanic inertial-range oscillations are excited at spatial scales of 500–1,000 km, but are liable to cascade down to scales comparable to the baroclinic deformation radius ($\sim$60km or 0.5° at 20S, 120 km at 10S) by a variety of mechanisms (Klein 2008). According to one definition, observed surface vorticity structures in the SEP have typical scales of 100–150 km (Chelton et al. 2007). The spectra of sea-surface height in the SEP area near 20S appear to peak near 500 km (Colbo and Weller 2007).

Advection associated with such small-scale structures cannot be accurately represented in current-generation standard-resolution coupled GCMs, where typical horizontal resolutions are 1–2° in the ocean. Moreover, virtually all current GCMs (including forecast models and reanalysis products; Cronin et al. 2006) tend to underestimate Sc cover and overestimate downwelling solar radiation. In spite of improvements in the last few years, the regional heat budget in coupled GCMs is still generally achieved via erroneously high SSTs, with associated errors in the seasonal cycle and in the large-scale surface winds (Yu and Mechoso 1999; de Szoeke and Xie 2007).

Recently, however, model simulations of better quality have become available. In one approach, Capet et al. (2008, 2009, in preparaion) use high-resolution regional ocean simulations to study the role of the eddies in the circulation, and to analyse the contributions to the heat budget of the upper ocean. Capet al. (2008) find that the rectifying mean advection from transients (i.e. the average of $u'\nabla T'$ over a period of several years) is significant, with localised positive and negative contributions at different depth, and a integrated heat flux over the upper 100 m of the oceanic column characterised by very small scales. These solutions are calculated for climatological surface forcings and boundary conditions derived reanalysis products, and the question is still open on how strongly such constraints affect the simulations.

In a second modelling approach, free-running, self-consistent multidecadal integrations of a coupled GCM have been carried out with higher resolution then previously in both the atmosphere (5/4° in latitude by 5/6° in longitude) *and* the ocean (1/3° $\times$ 1/3°, or about 30 km). The model, called HiGEM (Shaffrey et al. 2008, and references therein), derives from the new coupled GCM of the UK Met Office's Hadley Centre, HadGEM.

HiGEM produces a good simulation of the SEP climate (see also Sect. 2), and of tropical-Pacific variability (Roberts et al. 2009). In both these aspects there are remarkable improvements with respect to lower resolution models (including HadGEM), which crucially depend on the increased resolution of the ocean component (J. Donners, personal communication; Roberts et al. 2009). Although at 1/3° resolution HiGEM cannot resolve the oceanic dynamics on the scale of the deformation radius for latitudes higher than $\sim$10°, we will show that oceanic heat advection from transients in the simulation is consistent with existing estimates based on in-situ oceanographic data (Colbo and Weller 2007).

In the present paper we examine the spatio-temporal characteristics of oceanic heat advection in the SEP as simulated by HiGEM. At this stage, we do not address the question of how the characteristics of oceanic heat advection reflect on the SSTs. That would require the study of

the additional mechanisms by which sub-surface ocean stratification and dynamics affect the mixed-layer budget. Arguably, however, no such study can conclusively be carried out until the heat advection in the ocean column and its mechanisms are sufficiently understood, and the quality of model simulations of the regional oceanic circulation is known. Thus, for the time being, the focus is placed on the column heat budget.

Section 2 presents a short description of HiGEM and selected results from the integration. Section 3 is dedicated to the spatio-temporal characteristics of the model's oceanic temperature advection. Section 4 discusses the possible underlying physical processes for transient advection, and Sect. 5 presents our conclusions.

2 Model description and simulated SEP climatology

This study uses HiGEM1.2 (Shaffrey et al. 2008), which is derived from the latest climate configuration of the Met Office Unified Model, HadGEM1 (Johns et al. 2006; Martin et al. 2006; Ringer et al. 2006). The atmospheric component of HiGEM is based on a semi-Lagrangian, non-hydrostatic dynamical core on an Arakawa C grid (Davies et al. 2005), with horizontal resolution of 1.25° × 5/6° in longitude and latitude (N144), and 38 levels in the vertical. The parametrisations of planetary boundary-layer processes follows the non-local scheme of Lock et al. (2000), and is explicitly coupled with the mass-flux convection scheme. The latter incorporates a separate diagnosis of shallow and deep convection and a representation of convective momentum transport.

The ocean component has a horizontal grid-spacing of 1/3° in both longitude and latitude. In the vertical, there are 40 levels with smoothly increasing spacing from 10 m in the first few, near the surface, to near 300 m at depth. The maximum ocean depth is 5,500 m. The Eulerian advection terms are computed using a pseudo fourth-order scheme (Pacanowski and Griffies 1998) for tracers, and a second-order centred difference scheme for momentum. The external mode is solved with a linear implicit free-surface scheme (Dukowicz and Smith 1994), and salt and water fluxes are accounted for separately.

The details of the ocean physics parametrisations are given in Stevens et al. (2009), and here we only provide a brief summary. The vertical diffusivity at all depths follows a Richardson-number parametrisation, with a minimum background diffusivity which is depth-dependent for tracers and constant for momentum. The mixed layer is treated following the bulk equilibrium formulation of Kraus ant Turner (1967). Immediately below the mixed-layer base, the two formulations are matched by a local enhancement of the diffusivity. In the horizontal, lateral mixing of tracers is applied based on the isopycnal formulation of Griffies et al. (1998), with a constant isopycnal diffusivity. Also, to represent enhanced mixing at the ocean surface, tracers at levels 1 and 2 are mixed horizontally using a biharmonic scheme. In addition, at high latitudes noise in the tracers fields is reduced via adiabatic biharmonic diffusion (Roberts and Marshall 1998). The Boussinesq approximation for inertia is used with a reference density 1.035 g/cm^3, while buoyancy is derived from the equation of state of McDougall et al. (2003). Open-ocean convection is parametrised using the full convection algorithm of Rahmstorf (1993).

Like other low-resolution ocean models, HadGEM uses a Gent–McWilliams parametrisation (Gent et al. 1995) for isopycnal thickness diffusion to represent the effects of unresolved eddies. In HiGEM, the thickness diffusivity is set to zero, as tests showed that it gave no clear benefits with higher horizontal resolution, while resulting in reduced eddy variability and the erosion of fronts.

A seventy-year integrations of HiGEM1.2 was completed. The ocean was initialised from World-Ocean Atlas data for September 2001 (Conkright et al. 2002); the atmosphere was initialised from September ECMWF ERA-40 re-analysis (Uppala et al. 2005). For comparison, a parallel integration with HadGEM (version 1.2) was also carried out, with identical physics package in the atmospheric component. In this model, the resolution is 1.875° × 1.25° for the atmosphere, while the ocean has a constant resolution of 1° in longitude but a non-uniform meridional spacing with refinement equatorward of 30° from 1° to 1/3°.

In both models the top-of-the-atmosphere (TOA) radiation budgets, the atmospheric circulation, and the upper oceans reach equilibrium within the first few decades, although the abyssal ocean keeps adjusting from the initial conditions.

Figure 1 shows the mean October SSTs from the simulations and the observations. Like many current-generation models (IPCC 2007), HadGEM SSTs have a marked warm bias in the SEP. This is compounded by the cold bias in the central south and equatorial Pacific, related to the excessive strength of the trade winds, resulting in large errors in SST gradients. By contrast, South of the Equator there is good agreement between HiGEM and the observations, with the largest errors, located near the South-American coast, of the order of 1°C. West of 80W, SST errors are much smaller. Low-level cloud cover in HiGEM is higher than in HadGEM, and cloud reflectivity compares well with observations (Shaffrey et al. 2008). Nevertheless, some problems still persist despite the increased resolution. The simulated inversion at the top of the planetary boundary-layer (PBL) is too weak, and the cloud short-wave forcing may be a little too small, with a downwelling component at the surface of

210 W/m^2 at the IMET buoy's location (20S, 85W), larger than 194 W/m^2 (with an error less then 5 W/m^2) estimated by Colbo and Weller (2007). Consistently, long-wave, sensible and latent heat fluxes are all slightly excessive (in absolute values) than the measurements at the site of the IMET buoy. Also, amplitude in the mean seasonal cycle of net downward heat flux is a little too weak. Even so, its temporal characteristics are well captured, with net heat gain by the ocean between September and March, and smaller heat loss between April and August.

Figure 2 shows the simulated upper-ocean temperature and salinity profiles at the buoy's location together with in-situ data. Below the mixed layer, the simulation agrees reasonably well with the observations. There are small systematic differences mainly in the depth of the mixed layer (too shallow), in the thermocline structure (too diffuse), and in the second salinity maximum below 200m (too deep and diffuse). The salinity minimum is, however, present in the simulation, with the correct depth, and values close to the observed.

Finally, Fig. 3 shows snapshots of the near-surface ocean vorticity, and statistics for the sea-surface height from the simulation. These fields are characterised by features with small spatial scales and high relative vorticity typical of oceanic eddies. The power spectrum of sea-surface elevation follows a power law k^{-a}, with $a \sim 2.5$, down to scales of 250 km, and drops off sharply at higher wavenumbers.

A drop in the spectral energy-density at around 6–8 times the grid spacing is commonly observed in numerical models (D. B. Chelton, personal communication); it might be related with the inclusion of biharmonic diffusion in HiGEM, and it does not necessarily imply that smaller structures are not important. Nevertheless, the cut-off value we find compares favourably with the spectral peak around 500 km reported by Colbo and Weller (2007), or around 400 km as simulated in the high-resolution (1/9°) regional ocean model of Penven et al. (2005). In terms of observed eddy statistics, Chaigneau et al. (2008) report average eddy radii of 100 km at 20S, corresponding to a wave-length of 400 km. They also show that most EKE is associated with the larger, longer-lived eddies.

The westward motion of the sea-surface height structures (right-most panel in Fig. 3) is ∼4.5cm/s, also in line

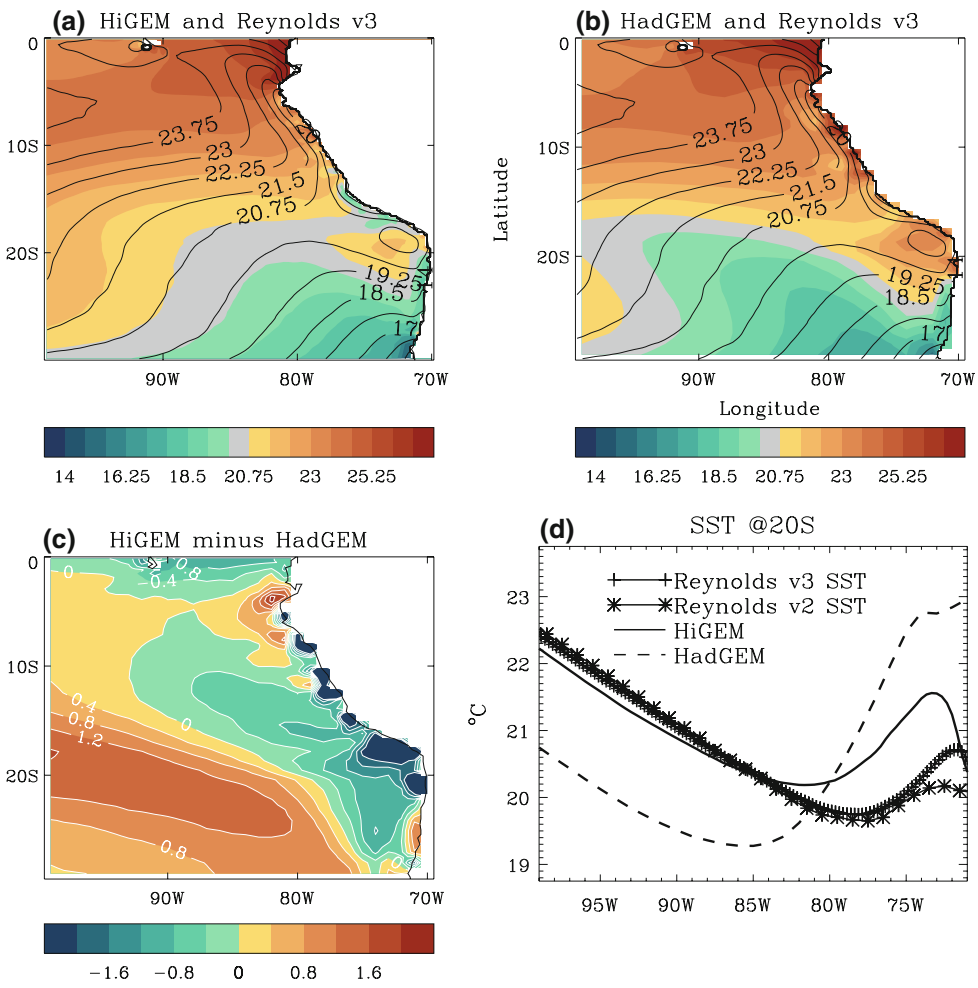

Fig. 1 Mean SSTs in the SEP. **a** HiGEM (*colour coding*) and Reynolds v3 (*contour lines*); **b** HadGEM (*colour coding*) and Reynolds v3 (*contour lines*); **c** differences between SSTs from HiGEM and from HadGEM; **d** Profiles along 20S for HadGEM (*dashed*), HiGEM (*dash-dotted*), and for two Reynolds SST datasets (see legend)

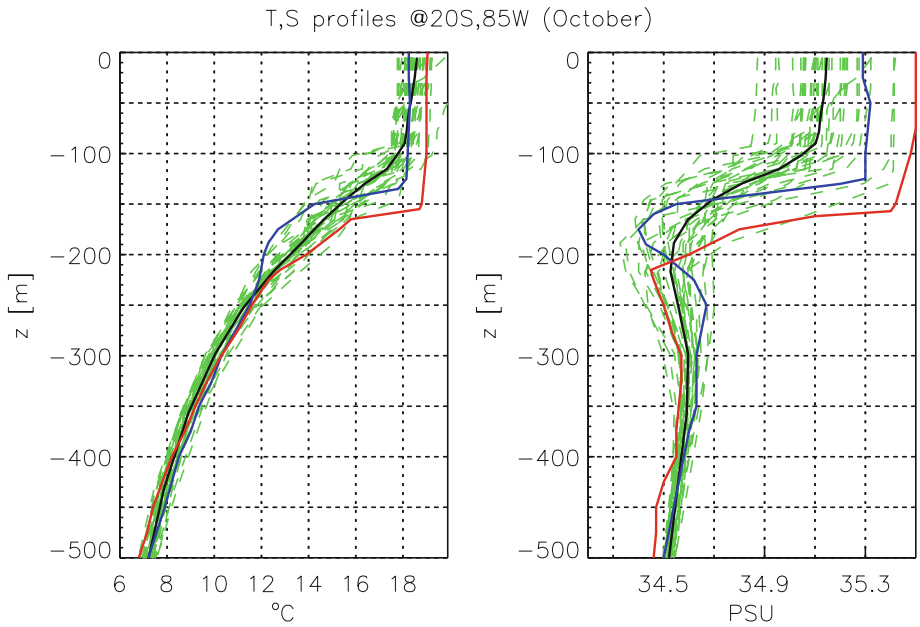

Fig. 2 Temperature (*left*) and salinity (*right*) profiles at (20S, 85W). The *thick black lines* show the 30-year average for 11 October from the HiGEM model. The *green broken lines* indicate T, S for on 11 October of the individual years in the simulation. The *blue and red lines* are from data taken with the IMET Buoy instrumentation, for 9 October 2000 and 18 October 2001, respectively (Colbo and Weller 2007)

with the observations for this region (S.-P. Xie, personal communication).

Evidence that some of these structures can be understood as transient eddies is given by the Okubo–Weiss (O–W) diagnostics as used, for example, in Chelton et al. (2007) or Penven et al. (2005). The O–W parameter is defined as the difference between the square of the deformation and the square of the vorticity, i.e.

$$\xi = \left(\partial_x u - \partial_y v\right)^2 + \left(\partial_x v + \partial_y u\right)^2 - \left(\partial_x v - \partial_y u\right)^2 \qquad (1)$$

and is suited to tracing eddies as they are characterised by large vorticity in their centre and large deformation at their edges. Figure 4 gives the statistics associated with negative local minima of the Okubo–Weiss parameter within the SEP region (threshold $-4\text{e}{-12}$ s^{-2}). For this calculation, a high-pass Fourier filter with cut-off at 13 grid-points (470 km) was applied to the sea-surface elevation data in order to isolate mesoscale structures from sharp features of the regional circulation. The derived eddy statistics are generally consistent with the findings of Chelton et al. (2007) and Chaigneau et al. (2008) from altimeter data. The O–W diagnostics gives an estimated mean eddy-diameter of about 130km, and on average the eddies propagate westwards while conserving their basic structural properties (size and central vorticity); anticyclonic ($\zeta > 0$) and cyclonic ($\zeta < 0$) eddies tend to propagate with positive and negative meridional velocity, respectively. At approximately 2.7 cm/s, the mean zonal propagation speed of identified O–W features appears to be lower than that of surface-height anomalies (Hovmüller diagram in Fig. 3), appears to be slightly lower than observed for eddies at similar latitudes (Chelton et al. 2007). Our statistics are affected both by weak, short-lived "point-eddies", for which the O–W diagnostics may not be suitable (see also Chaigneau et al. 2008), and by a number of eddies which are nearly stationary and tend to be have large amplitude. The number of O–W features that do propagate at the observed speeds in excess of 3.5 cm/s (cf. Figure 4 in Chelton et al. 2007) is small. Our values may compare a little more favourably with the results of Chaigneau et al. (2008), who give a mean propagation speed of 3 cm/s for eddies at 20S. In any case, the vorticity and O–W diagnostics together imply that some of the relevant range of observed eddies is active in this model.

3 Mean and transient oceanic heat advection

In the calculations for the present analysis we used 29 years of instantaneous 3-D data fields at intervals of 5 days from the HiGEM integration.

The upper-ocean column-integrated temperature advection is defined as $\int \mathrm{d}z\ (-u\cdot\nabla T)$, where u and ∇ are the three-dimensional current and gradient operator respectively and the integral is computed between $z = 0$ and $z = -477$ m, corresponding to the top 20 model levels. Results obtained when including one more level are practically identical on the time-scales of interest here. In the following, we express the column-integrated heat advection tendencies as equivalent surface fluxes in W/m^2 by multiplying by the specific heat per unit volume, ρc_p. For ease of notation, we shall generally refer to the integrand only, assuming integration and scaling (except for Fig. 13 where explicit reference needs to be made to the vertical

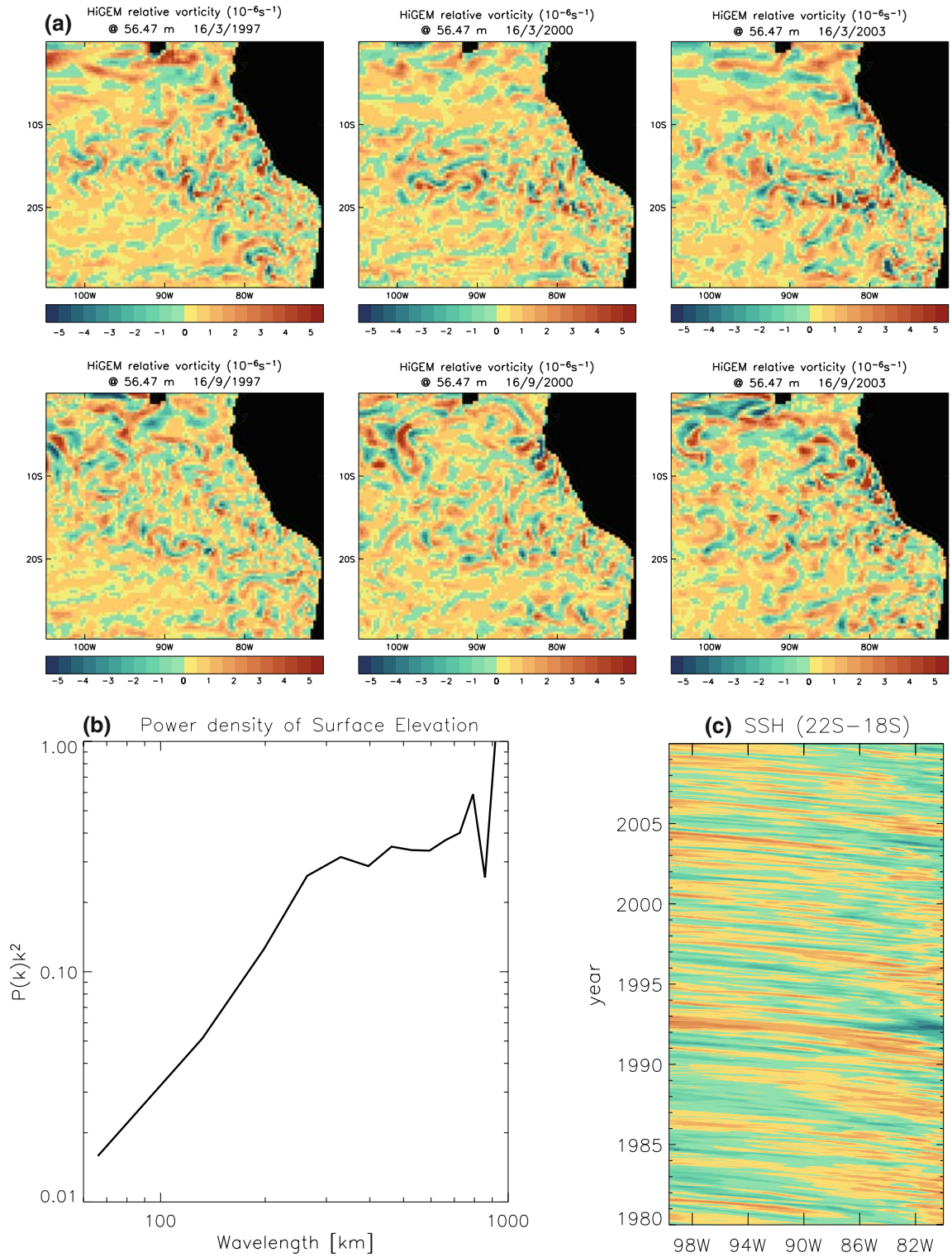

Fig. 3 **a** Snapshots of the relative vorticity fields in the SEP at $z = -56$ m from the HiGEM integration, taken from three different model years (*columns*) on 16 March (*upper row*) and on 16 September (*lower row*). The units are 10^{-6} s. **b** Average spatial spectral power density of the ocean surface height field for 30 years of the integration. A cut-off is seen at about 250 km (8 grid-points). **c** Longitude-time Hovmüller contour-plot of sea-surface height averaged between 22S and 18S. The contour interval is 0.6 cm. Time increases upwards

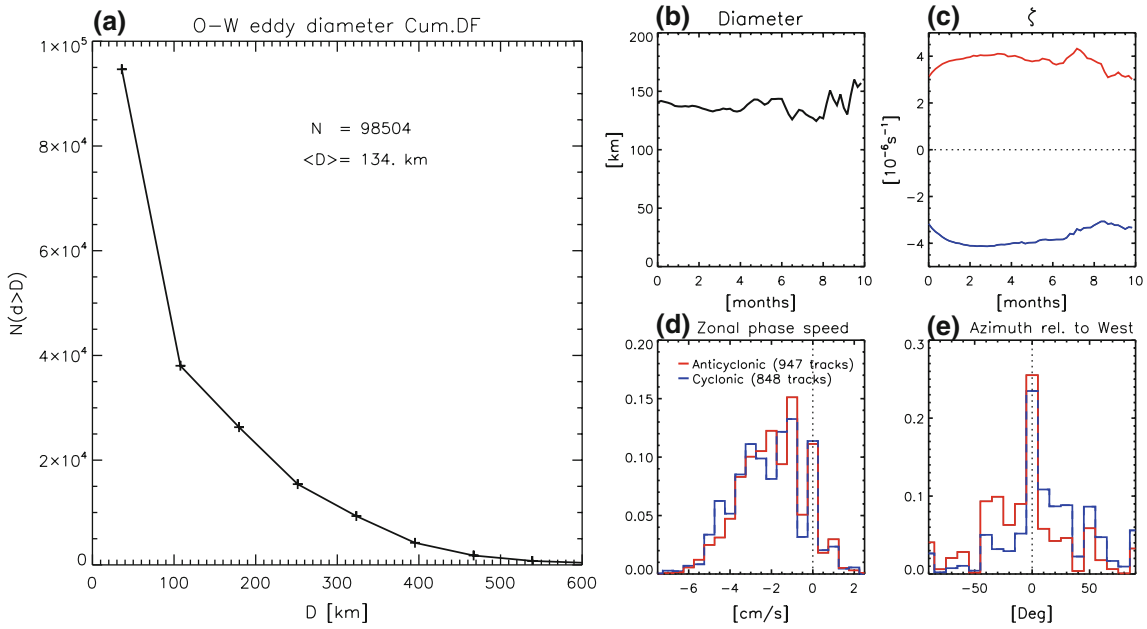

Fig. 4 Statistics derived from the Okubo–Weiss parameter, ξ, for the properties of eddies in the SEP in the HiGEM model. **a** Cumulative distribution of diameters of all features within the SEP (105W–75W, 24S–15S) having a central O–W value $\xi < -4 \times 10^{-12}/\mathrm{s}^2$. The diameter D is defined as twice the distance from the minimum at which the average $\xi = 0$. **b** Average eddy diameter as a function of age. **c** Average evolution of eddy central vorticity ζ as a function of its age. **d** Histogram of zonal propagation speed for cyclonic (*blue*) and anticyclonic (*red*) eddies with origin between 22S and 18S. The frequency-distribution functions are normalised to 1, and the total number of tracks in each case is given in the legend. **e** For the same eddy populations, histogram of mean propagation angle relative to due west (positive = poleward)

structure and the temperature advection tendency is given in W/m^3).

The total mean advective tendency is the long-term average of $-u{\cdot}\nabla T$. This can be decomposed into a part attributable to the long-term mean circulation, and a part attributable to anomalies, i.e. departures from the long-term mean. We thus write:

$$-\overline{u \cdot \nabla T} = -\overline{(\overline{u} + u') \cdot \nabla(\overline{T} + T')} = -\overline{u} \cdot \nabla \overline{T} - \overline{u' \cdot \nabla T'}, \tag{2}$$

where $\overline{x}$ indicates the long-term average of x and use is made of $\overline{x'} = 0$. The contribution to the mean advection from anomalies is, therefore, given by the vertical integral of $-\overline{u \cdot \nabla T} + \overline{u} \cdot \nabla \overline{T}$. This quantity is shown for a section along 20S as the red line in Fig. 5, together with the total advection $-\overline{u \cdot \nabla T}$ (dark blue line), the advection implied by the mean fields, $-\overline{u} \cdot \nabla \overline{T}$ (green line), and the mean downward surface heat flux (black line) from latent and sensible heat and short-wave and long-wave radiative components.

As discussed above, in the annual mean the ocean column gains heat from the incoming solar radiation, which is only partially reflected by clouds. The other surface-flux components, foremost evaporation, which are all negative, do not fully compensate the short-wave heating. In the long-term average, the local budget must be closed by cold

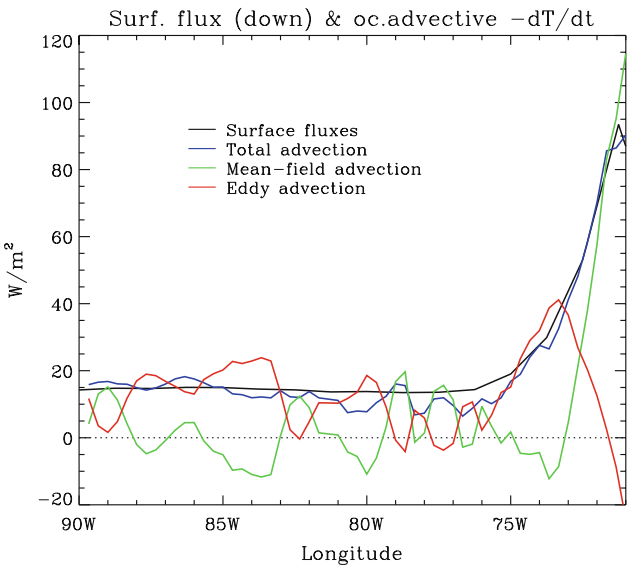

Fig. 5 Components of the ocean-column heat budget along 20S in the SEP. The mean downward surface flux (*black line*) is approximately balanced by the total mean advection (*dark blue line*; sign inverted). The latter is decomposed into a mean advection component (*green line*) and an advection component from anomalies (*red line*)

oceanic advection, exporting heat to other parts of the ocean (mostly westwards and polewards). Figure 5 shows this to be approximately the case. The residuals provide an

estimate for long-term model drifts, and for the accuracy of our calculation, which neglects horizontal diffusion. In the region of large gradients near the coast, these errors can be as large as 6.5 W/m^2; elsewhere, they are less than 3 W/m^2. Figure 5 also shows that, at this particular location (20S, 85W), transients dominate the long-term balance, with smaller contributions from advection of the long-term mean temperature by the long-term mean currents. In the model, the heat advection from anomalies at the location of the IMET buoy is about -20 W/m^2, consistent with the observational estimate of Colbo and Weller (2007), which varies between -30 ± 12 and -20 ± 11 W/m^2.

In order to understand the physical meaning and the climatological consequences of this apparent match, we proceed to characterise the spatio-temporal properties of the variability associated with heat advection as represented in the model.

A significant role for the non-steady part of the circulation may be expected, since both the seasonal cycle and interannual anomalies associated with the El-Niño/Southern Oscillation (ENSO) have large amplitudes in the SEP. The question is which of the various sources of variability generates transient heat advection with a non-vanishing long-term mean. In general, different mechanisms will be characterised by different spatial and temporal scale. For example, the wind-driven Ekman circulation is characterised, like the winds themselves, by relatively short temporal scales and relatively large spatial scales. By contrast, the geostrophic subduction of surface-temperature or surface-salinity anomalies will occur on annual time-scales or slower, and will be associated with displacements of the thermocline or with temperature and salinity fronts. We have also shown that structures of small spatial scale resembling mesoscale eddies are simulated in HiGEM.

In order to isolate the spatial and temporal scales of the flow associated with rectifying transient advection, we split the ocean currents and temperatures into distinct temporally and spatially filtered components:

$$-u' \cdot \nabla T' = -(u'_1 + u'_2) \cdot \nabla (T'_1 + T'_2) \qquad (3)$$

where subscripts indicate orthogonal components in either time or space. In the case of time-filtering, the advective tendency the cross-terms between different components vanish in the time-mean, i.e. $-\overline{u' \cdot \nabla T'} = -\overline{u'_1 \cdot \nabla T'_1} - \overline{u'_2 \cdot \nabla T'_2}$.

A first decomposition is shown in Fig. 6, where u'_1, T'_1 are taken as monthly departures from the long-term mean of the mean seasonal cycle, and u'_2, T'_2 are the anomalies with respect to mean seasonal cycle. Two properties of the advection field immediately stand out. First, the spatially smooth long-term mean total advection is the sum of two spatially "noisy" components, one attributable to the mean circulation, $-\overline{u} \cdot \overline{T}$, and the other to a residual mean from the interannual anomalies. Second, among the time-varying components, the mean seasonal cycle does not rectify onto a significant advective contribution, except near the coast and near the Equator. The small-scale spatial pattern apparent in $-\overline{u} \cdot \overline{T}$ is somewhat surprising considering the smoothness of its factors. To some degree, the advective tendencies generated from anomalies act to cancel those small-scale features and bring the column energy budget back into balance with the spatially smooth surface fluxes. Also, the simulated advection associated with transients does not cool the ocean everywhere, but exhibits a broad, zonally oriented cooling/warming dipolar structure along 17S.

We further split the time-varying component of the current and temperature fields, $u - \overline{u}$ and $T - \overline{T}$, into Fourier bands of different frequencies by applying, point by point, low-, band- and high-pass Fourier filters to the data time-series. The results (Fig. 7) show that the anomalies associated with mean oceanic heat advection are predominantly characterised by time-scales comparable to the annual cycle ("inter-seasonal"), although transients with longer, i.e. inter-annual, periods cannot be neglected.

At the location of the IMET buoy, inter-seasonal and inter-annual anomalies both contribute to the "eddy" heat advection (Fig. 8). The contribution of transients with periods less than 4 months is generally negligible.

The persistence of small-scale structure in the oceanic heat advection is visually exemplified in Fig. 9 which shows annual-average advection totals ($\overline{u \cdot \nabla T}$, where by the bar we now intend an average over one year only) and means ($\overline{u} \cdot \nabla \overline{T}$) for nine consecutive years of the simulation. Even on annual time-scales, the small-scale features present in the total advection heat tendencies are not matched by similar ones in surface fluxes, which are spatially much smoother. Annual-mean heat-budget surplus or deficit of the order of 20 W/m^2 over small areas are common.

Applying spatial high-pass Loess filters (Schlax and Chelton 1992) shows that the small-scales features in the long-term mean oceanic heat advection are almost entirely generated by anomalies with characteristic spatial scales of less than 500 km (Fig. 10). An even higher filter cut-off of 6 grid-point ($\sim$200km) yields a noticeably weaker, but still recognisable contribution, suggesting that there is still variability associated with the smallest spatial scales resolved numerically on the model's grid.

4 Generation of rectifying transient heat advection

Consistently with the properties of atmospheric variability, variations in the oceanic column heat budget have temporal characteristics similar to those of surface-flux anomalies in

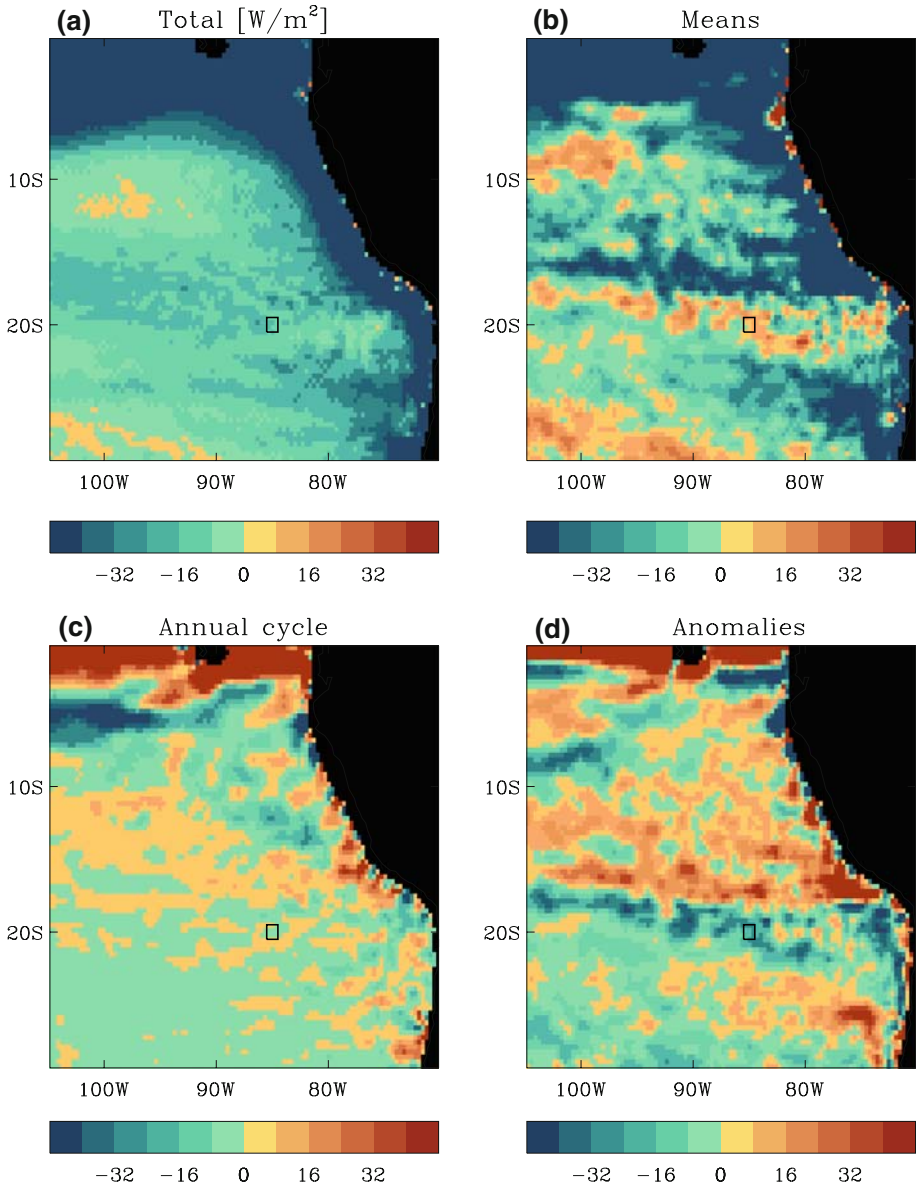

Fig. 6 Maps showing (**a**) the model 20-year mean, total heat advection in the upper ocean (0–500 m), and the partial contributions from (**b**) heat advection by the mean fields, from (**c**) the anomalies, with respect to the long-term mean fields, of the average seasonal cycle, and from (**d**) the remaining anomalies. The *box drawn* in each map represents the location of the IMET buoy (Colbo and Weller 2007)

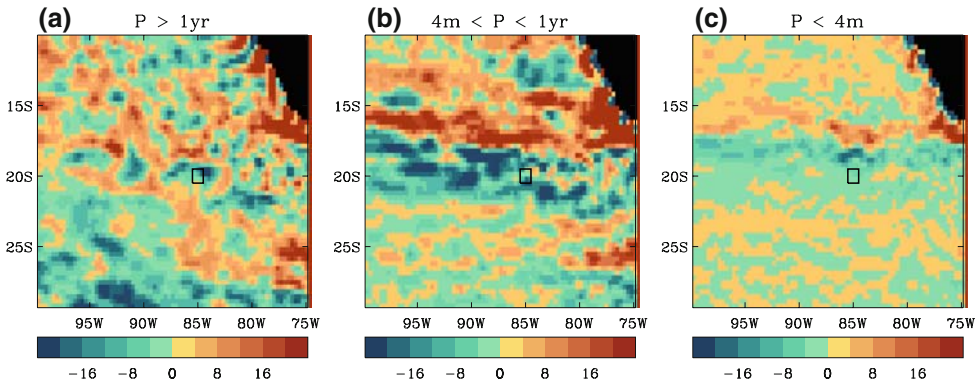

Fig. 7 Similar to Fig. 6, further decomposition of ocean heat advection from anomalies into contributions from anomalies low-, band-, and high-pass filtered in time, in panels (**a**), (**b**) and (**c**) respectively. The residual from the cross-terms of the Fourier components is non-vanishing due to FFT aliasing of the finite time-series, but it is very small

the high-frequency part of the spectrum over large spatial domains (Fig. 11c, d). At longer temporal scales, the temporal spectrum of the heat-budget changes follows more closely that of the advective tendencies. At smaller spatial scales also the high-frequency association between the heat budget and surface fluxes is lost (Fig. 11a, b).

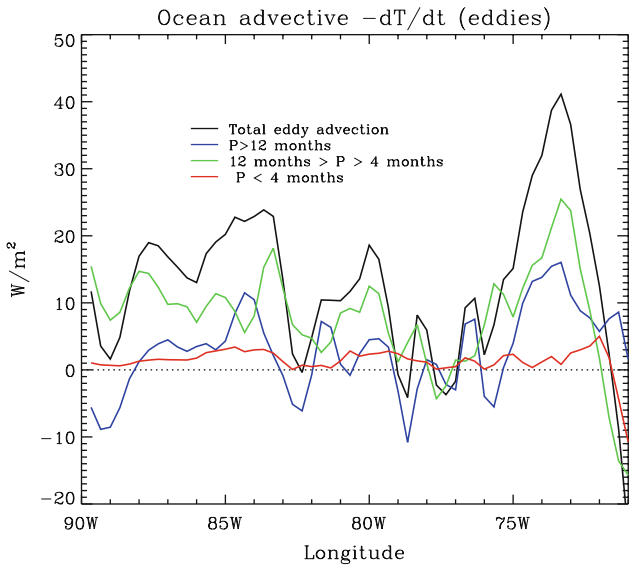

Fig. 8 Total mean advection (*black line*) along 20S in the SEP. This is decomposed into advection by anomalies with time-scales of less than 4 months (*red line*), of between 4 and 12 months (*green line*), and of longer than one year (*blue line*). See text and Fig. 7

Identical considerations apply to the wind-driven Ekman flow. In general, anomalies in the surface fluxes or in Ekman advection do not correlate with the ocean heat budget over the temporal scales (>4 months) and spatial scales (<500 km) which characterise rectifying advection transients (not shown).

The Ekman flow was estimated by fitting the surface currents to an Ekman spiral for the given wind-stress at each location and for each pentad-mean, giving an Ekman depth. Although this estimate was found to be consistent and useful for interpretation, it is not rigorous.

Geostrophic velocities, by contrast, could be calculated at each time from the temperature and salinity fields via the equation of state, the sea-surface elevation and hydrostatic balance. Geostrophic temperature advection was then computed from these currents, assuming $\nabla \cdot u = 0$, and split into components in different frequency bands. Figure 12 shows the result of this decomposition and can be directly compared with Fig. 7. The results confirm that rectifying temperature advection from transients is mostly attributable to geostrophic flow anomalies. Furthermore, we have verified that anomalies in the vertical component of the flow give a negligible contribution almost everywhere.

This has immediate implications which we discuss in the following. Our aim is to understand the origin of the correlations between the local geostrophic currents and the local gradients in temperature that give raise to the rectifying advection from transients, i.e. to the non-zero mean for $u_g' \nabla T'$. Such correlations are not obvious; at the same time the pattern of $\overline{u_g' \nabla T'}$ is localised in a preferential area, in two broad bands between 20S and 15S.

First let us inspect the temperature and salinity structure of the ocean near the IMET buoy's location at 20S, 85W (Fig. 13). The region is characterised by an intrusion at depth, just below the thermocline, of fresh water from higher southern latitudes. This large-scale feature in the SEP is well-documented (see e.g. the World Ocean Atlas; Conkright et al. 2002). Within the thermocline, the density gradient associated with the salinity field has a positive vertical component in this region, but a possible instability to mixing by salt fingering is not represented in the model.

The distribution of heat advection (indicated by the colour-coding in Fig. 13, see caption) suggests that transients are particularly important at the edge of the intrusion, where ∇S and ∇T turn out of alignment with each other. Considering the sharpness of the thermocline and of the halocline (which is very pronounced in actual, instantaneous fields, compared with the time-averages shown here), and the negligible contribution to transients from vertical advection, we interpret this in the following way.

The geostrophic current is given by $u_g = 1/(\rho f)\hat{\mathbf{z}} \times \nabla_h p$, where ρ is the density (assumed constant in the inertial terms), f is the Coriolis parameter, $\hat{\mathbf{z}}$ is the upward-pointing unit vector, p is the pressure, and ∇_h is the horizontal gradient operator. From hydrostatic balance,

$$\nabla_h p = g \nabla_h \int \rho \mathrm{d}z = g \int (\beta \nabla_h S - \alpha \nabla_h T) \mathrm{d}z \tag{4}$$

$\alpha := -\partial\rho/\partial T$ and $\beta := \partial\rho/\partial S (\alpha > 0, \beta > 0)$. Note that, here and in the following, we neglect anomalies in the sea-surface heights, since we are only interested in local current anomalies that correlate with local temperature and salinity anomalies. The horizontal temperature advection from geostrophic currents is then written as:

$$u_g \cdot \nabla_h T = \frac{g}{\rho f} \left[\int \beta \nabla_h S \mathrm{d}z \right] \times \nabla_h T - \left[\int \alpha \nabla_h T \mathrm{d}z \right] \times \nabla_h T. \tag{5}$$

The terms on the right-hand side of Eq. 5 give a non-zero contribution if the isohalines intersect the isotherms (there is "spiciness"), or the isotherms turn with depth. Both conditions are verified in the SEP. Figure 13a shows that both the thermocline and the halocline are sharp and sloping. Moreover, Fig. 13b shows that the turning of the isohalines towards the vertical in coincidence with the termination front of the fresh intrusion also provides a configuration where the horizontal density gradient increases just below the thermocline at $z \sim -200$. We can idealise the situation depicted in Fig. 13 by assuming that there is an upper ocean layer above the thermocline where $\nabla_h S_s \parallel \nabla_h T_s$ (where the subscript indicates upper-layer quantities),

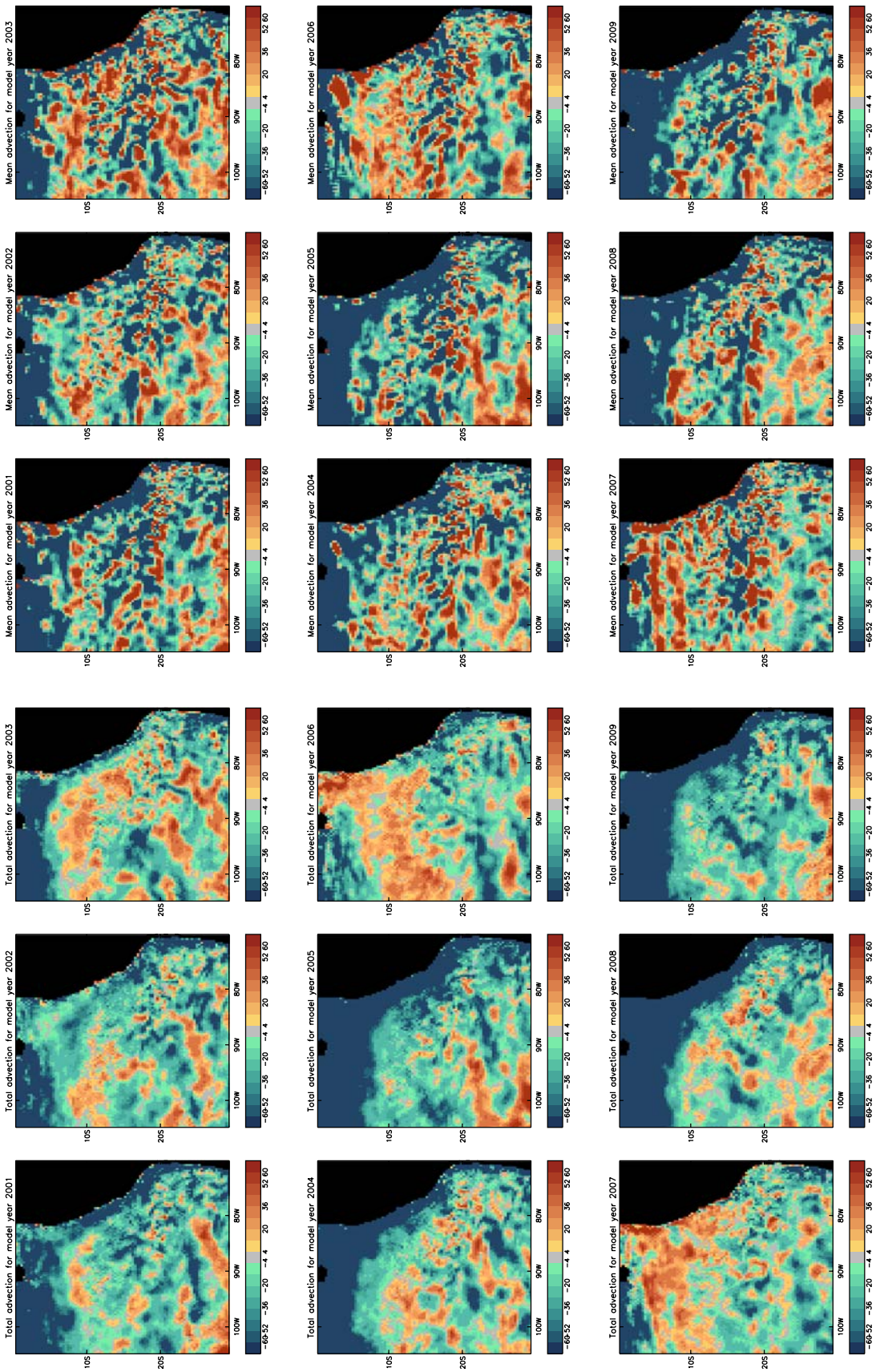

Fig. 9 Two sets of nine panels showing the spatial maps of the annual means of the total heat-advection tendencies (nine panels on the *right-hand side*) and the annual mean-field heat-advection tendencies (nine corresponding panels on the *left*) for nine consecutive years of the integration (2001–2009 in model time)

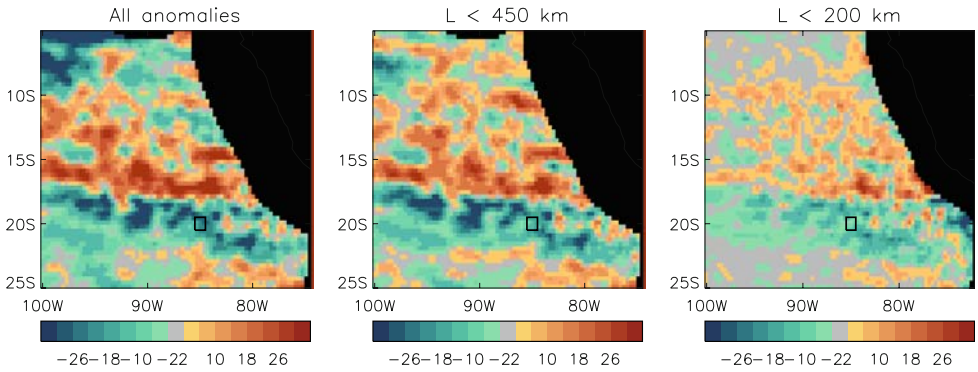

Fig. 10 Total mean advective heat tendencies from anomalies (first panel from the *left*), and from anomalies with spatial scales of less than 13 model grid-points (∼450 km, *middle panel*) and of less than 6 grid-points (∼200 km, *right-most panel*)

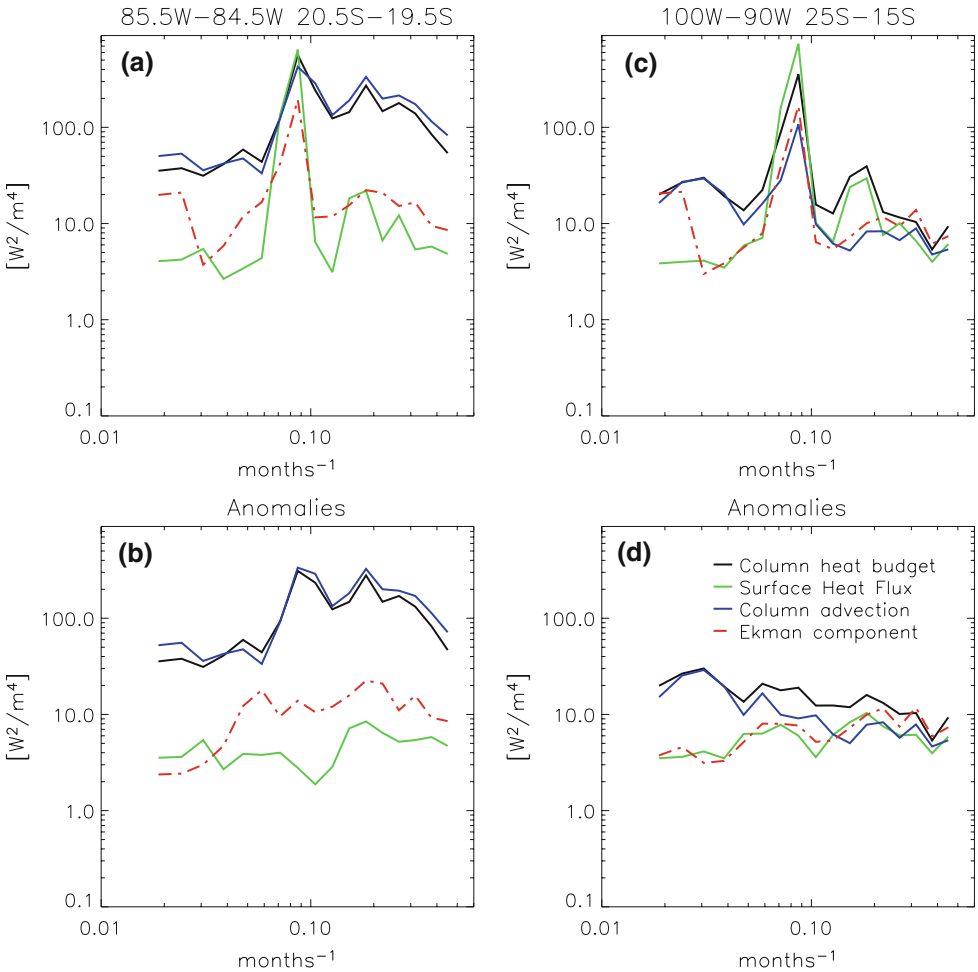

Fig. 11 Power spectra of heat budget, surface fluxes, and total and Ekman advection averaged over two areas in the SEP, a 1° × 1° box in panels **a** and **b**, and a 10° × 10° box in panels **c** and **d**, as indicated. The *upper panels* (**a**, **c**) show the spectra for the totals, the *lower panels* (**b**, **d**) for the anomalies

and a lower ocean layer, beneath the thermocline, where $\nabla_h T$ turns out of alignment with both. At a depth z in the deeper layer the two terms on the right-hand side of Eq. 5 can be thus approximated as:

$$u_g \cdot \nabla_h T \approx \frac{\beta g}{\rho f} \Delta z (\nabla_h S \times \nabla_h T) - \frac{\alpha g}{\rho f} \Delta z_s (\nabla_h T_s \times \nabla_h T), \quad (6)$$

where Δz and Δz_s represent the thicknesses of the deep and upper layer, S and T are deep-layer salinity and temperatures, and T_s is the upper-layer temperature. (Note that there should also be a term in S_s analogous to the that in T_s; but assuming $\nabla_h S_S \| \nabla_h T_s$ this can be effectively incorporated in the T_s term). In order to study rectifying transients in geostrophic ocean temperature advection, Eq. 6 can be applied to the anomalies, i.e.

$$-u_g' \cdot \nabla_h T' \sim a(\nabla_h S' \times \nabla_h T') - b(\nabla_h T_s' \times \nabla_h T'), \quad (7)$$

where a and b are positive constants ($f < 0$). We note that for the anomalous geostrophic advection of salinity there is a term identical to the first in Eq. 7, with a different

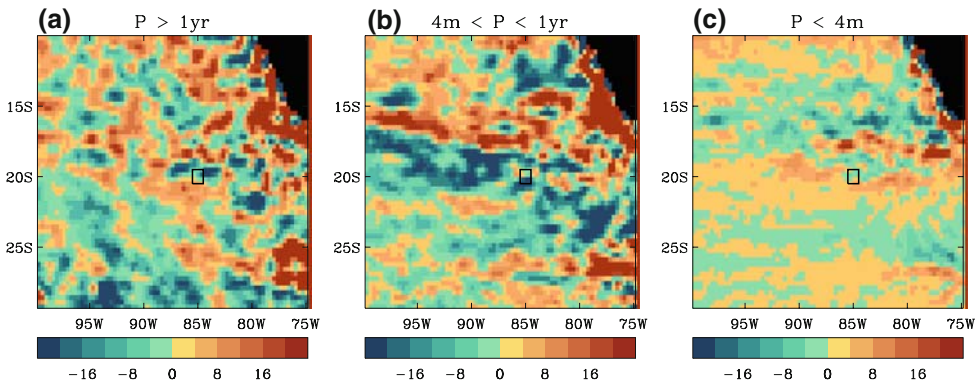

Fig. 12 Similar to Fig. 7, for advection from geostrophic currents only

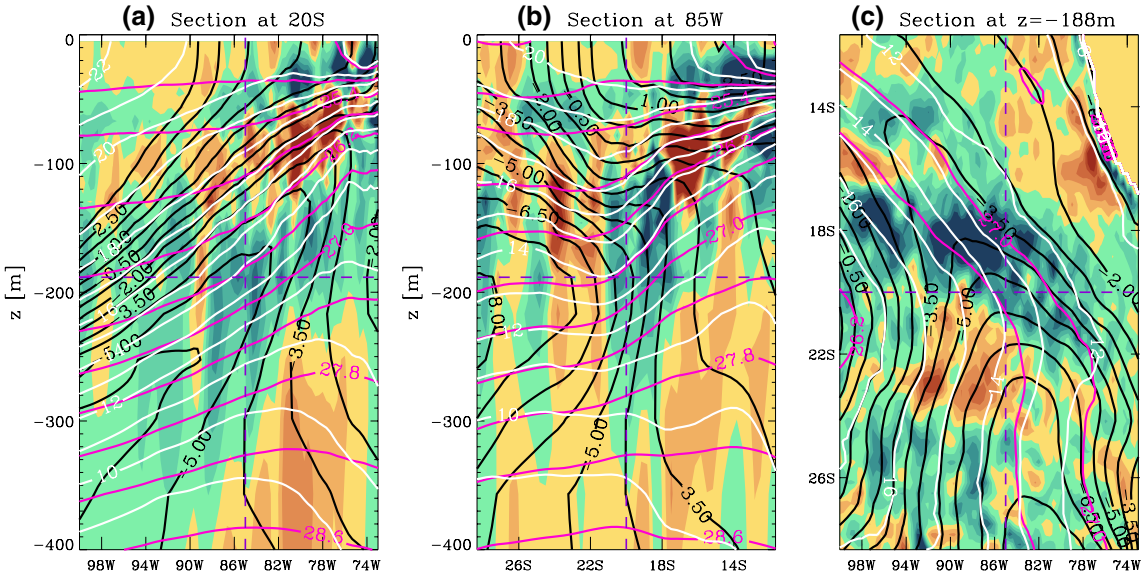

Fig. 13 Sections showing heat-advection tendencies, in W/m^3, from (total) transients, in filled *colours*. Contour interval is 0.04 W/m^3, with *deep red* indicating values in excess of 2 W/m^3 and *deep blue* indicating values less than −2 W/m^3. *Line contours* represent the temperature field, in *white* (contour interval 1°C); the salinity, in *black* (units of (PSU-35)*10, contour interval of 0.075 PSU); and the density, in *purple* (units of kg/m^3—1,000, contour interval of 0.4 kg/m^3). **a** Depth-longitude section along 20S. **b** Depth-latitude section along 85W. **c** Planar section at constant depth, z = −188 m

positive constant as β is replaced by α in the first term on the right-hand side of Eq. 6.

We have evaluated the two terms on the right-hand side in Equation 7 from HiGEM data at the IMET buoy's location. In Fig. 14, they are plotted together with the vertically integrated, horizontal temperature advection from geostrophic current anomalies, calculated directly as $\Theta_g = \int -u_g' \cdot \nabla_h T' \mathrm{d}z$. It is confirmed that they provide useful estimates of anomalous advection at that location. They both rectify to negative values (cold advection), as Θ_g does, and their correlation with Θ_g are equal to 0.43 and 0.49, respectively, which are highly significant values for the 1,440 time-points considered. For each, we chose the level with the best correlation with Θ_g, and it is interesting to note their slightly different depths; but correlations are equally significant for all levels between 200 and 300 m, where both the misalignments in the gradients and the currents are large. Among all estimators that can be based on Eq. 5, these are the best, in accord with the above interpretation. Fluctuation in the upper-ocean salinity S_s' are not well correlated with T_s', but they are smaller and have a small effect on the density and pressure. The salinity perturbation at depth, by contrast, are large, and well-correlated with temperature. In fact, the biggest contributions to T_s' do not arise at the surface with, but rather at the level of the mean thermocline. In particular, the "shallow" layer characterised by T_s is in fact the thermocline between 120 and 200 m of depth, adjacent to the "deep" layer. All this phenomenology appears to be determined by the presence of the fresh intrusion. Shown in

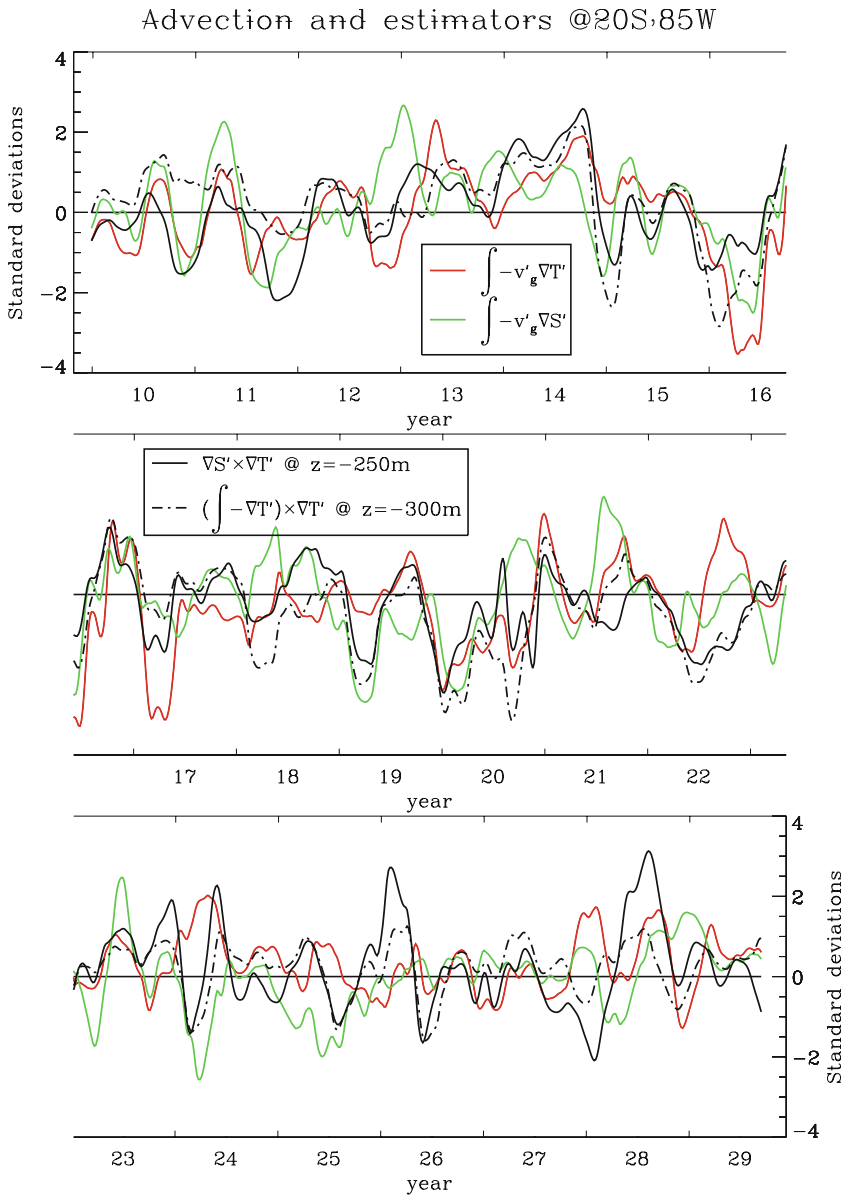

Fig. 14 Time-series of the anomalous, rectifying, horizontal geostrophic temperature and salinity advection (*red and green lines*, respectively) and the two estimators of Eq. 7 (*black solid* and *dash-dotted lines*, respectively). Note that the times-series continues across the three panels. The *curves*, which are based on pentad-frequency data, have been smoothed for easier reading before plotting. See text for discussion

Fig. 14 is also the vertically integrated anomalous salinity advection, $\Sigma_g = \int -u'_g \cdot \nabla_h S' \mathrm{d}z$. It also correlates positively with both Θ_g and $(\nabla_h S' \times \nabla_h T')(c \simeq 0.3)$, as expected. The magnitude of the two estimators is also realistic. Inserting the coefficient of Eq. 6, with a typical values for $\alpha \simeq 10\,\mathrm{kg/m^3}/$ PSU, $\beta \simeq 30\,\mathrm{kg/m^3/K}$, and $\Delta z \simeq 100$ m, the averages and standard deviations of the two estimators $\sim 10^{-5}$ K/s for the depths considered, within a factor of 2–3 of the values for Θ_g.

In the following, we discuss the possible mechanisms generating advection anomalies of the form (7) which rectify in the mean. We focus on the $\nabla_h S' \times \nabla_h T'$ term, keeping in mind that all considerations apply equally to the $\nabla_h T'_s \times \nabla_h T'$ term, as long as it is allowed that the perturbations considered affect the deep and the thermocline layer with perturbations of the same sign. Our task therefore reduces to considering mechanisms which generate correlations between $\nabla_h S'$ and $\nabla_h T'$. We hypothesise that such correlations arise from perturbations of the frontal structure associated with the fresh intrusion, which cause changes in either the position and intensity of the front, or perturbation in the front structure itself. Let us consider each case in turn.

From the T, S fields depicted in Fig. 13c, a displacement of the water-mass associated with the fresh intrusion near the salinity front at 20S, 85W tends to generate a negative correlation between S' and T'. If we assume the fronts dividing the water-masses in the horizontal plane to be very

sharp, as in the cartoon of Fig. 15a, with $f < 0$, a negative angle between $\nabla_h T$ and $\nabla_h S$ generates a cold advection anomaly at the front intersection during the displacement. Note that a displacement opposite to that shown in Fig. 15a will simply change the signs of all anomaly gradients, resulting in advective anomalies of the same sign. Conversely, a change in sign of the temperature gradient across the front will be associated with advective anomalies of the opposite sign. (An example of such a configuration can be seen near 22S, 77W in Fig. 13c).

We hypothesise temporary displacements of existing oceanic fronts by "exogenous" advection not associated with local (i.e. localised in depth) perturbations in temperature and salinity. The conceptual mechanism we propose thus involves a two-step process with first-order, non-rectifying advective perturbations which generate the correlated T', S' anomalies that finally rectify in the mean. The perturbations can originate in the column above the relevant depth; for example in association with baroclinic eddies.

An alternative, slightly more elaborate, and probably more realistic form of this conceptual mechanism is sketched in Fig. 15b. In this case the displacement of water masses does not need to be large compared to the width of the front, and the correlations between $\nabla_h S'$ and $\nabla_h T'$ are assumed to originate from the advection field of an eddy-like kinematic feature. One can formalise this case by assuming background temperature and salinity fields of the form $T = G_T(0, y)$ and $S = G_S(x, 0)$, where $\nabla T = G_T \hat{\mathbf{y}}$ and $\nabla S = G_S \hat{\mathbf{x}}$ are assumed constant. By Eq. 6, the temperature advection from the mean geostrophic flow is proportional to $G_T G_S / f$. (As discussed before, we can make the special case that the second term is zero). The eddy-like feature is represented by a height field of the form $E = \varepsilon H(s)$ where $s = s(x, y, t) \equiv [(x - ct)^2 + y^2]/(2R^2)$, c is the zonal propagation speed of the eddy, R its radius, and ε its central height (which can be negative). The non-dimensional function $H(s)$ is assumed to be positive, integrable, and monotonically decreasing with respect to its argument s. The eddy currents are then given by $\mathbf{v}_e = (g\epsilon/fR^2)[-yH', (x - ct)H']$, where the single quote indicates the derivative, i.e. $H'(s) = dH/ds$. These generate anomalous temperature and salinity advection resulting in the following anomalies:

$$S' = -\int_{-\infty}^{t} \mathbf{v}_e \cdot \nabla S \mathrm{d}t' = G_S \frac{g\epsilon}{fR^2} y \int_{-\infty}^{t} H'(s') \mathrm{d}t' \tag{8}$$

$$T' = -\int_{-\infty}^{t} \mathbf{v}_e \cdot \nabla T \mathrm{d}t' = -G_T \frac{g\epsilon}{fR^2} \int_{-\infty}^{t} (x - ct') H'(s') \mathrm{d}t' = G_T \frac{g\epsilon}{fc} H(s) \tag{9}$$

Here, $s' = s(x, y, t')$, and in the last equality use has been made of $\partial H(s)/\partial x = (x - ct)/R^2$ $H' = -1/c$ $\partial H'/\partial t$ and $H(s) \to 0$ $(s \to \infty)$. We can now compute the second-order term of the eddy geostrophic temperature advection as proportional to

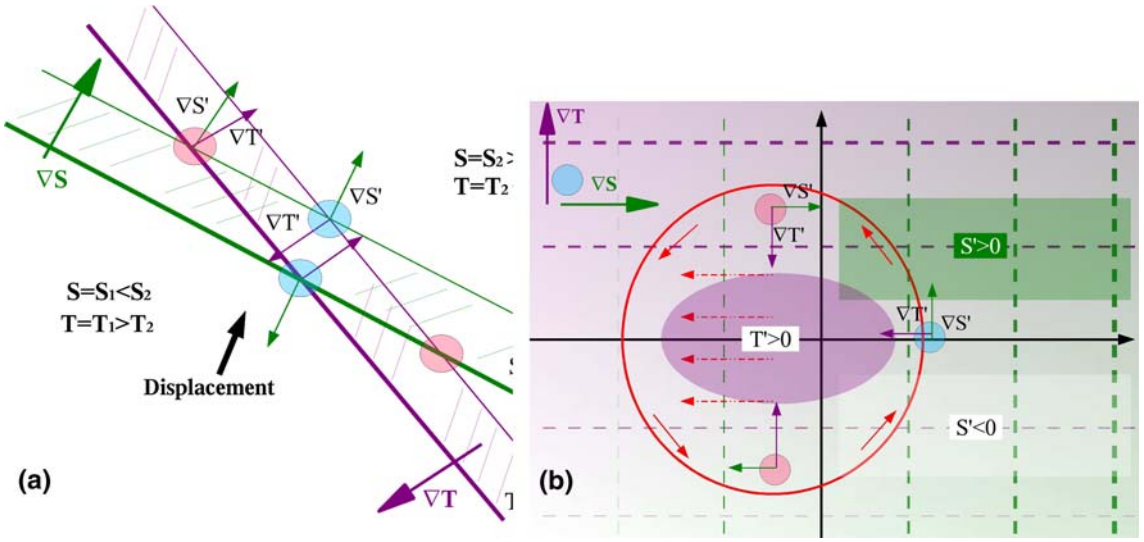

Fig. 15 Schematics of anomalies in the horizontal, geostrophic temperature advection field associated with a displacement of the salinity front near 20S, 85W. The *blue* and *pink areas* indicate localised cold and warm advection anomalies, respectively. See text for discussion

$$\frac{1}{f}(\nabla_h S' \times \nabla_h T') = \frac{G_T G_S}{f}\left(\frac{g\epsilon}{fR^2}\right)^2 \cdot \left\{ -\frac{y^2}{c^2}(H')^2 + \left(t - \frac{x}{c}\right) \times \left[H' \int_{-\infty}^{t} H'(s')\mathrm{d}t' + \frac{y^2}{R^2} H' \int_{-\infty}^{t} H''(s')\mathrm{d}t' \right] \right\} \tag{10}$$

In the time mean, as expected, this term does not average to zero. For $x = 0$ we obtain

$$\int -\mathbf{v}' \cdot \nabla T' \mathrm{d}t \sim \frac{G_T G_S}{f}\left(\frac{g\epsilon}{fRc}\right)^2 \times \left[\int_{-\infty}^{\infty} Q(s)\mathrm{d}r - \frac{y^2}{R^2} \int_{-\infty}^{\infty} -Q'(s)\mathrm{d}r \right], \tag{11}$$

where the function $Q := -(H^2/2)'$ and $s = r^2/2 + y^2/2R^2$. Since H^2 is monotonically decreasing, $Q > 0$, and the induced temperature advection anomaly along the path of the eddy centre rectifies with the same sign as the background mean advection. For most smooth eddy profiles $E(x, y)$, such as Gaussian or Lorentzian, $H'' > 0$ and $Q' < 0$, so that the second integrand is also positive definite. In the case of a Gaussian eddy, for example, we have $H(s) = \mathrm{e}^{-s}$, $Q(s) = \mathrm{e}^{-2s}$, so that the first integral is equal to $\sqrt{\pi/2}\exp(-y^2/R^2)$, and the second to twice that value. In general, however, for any choice of H, integration over y of Eq. 11 shows that all contributions exactly compensate, i.e. in the time-mean the advection from these transients vanishes when averaged over the whole domain. Equation 11 thus shows that the passage of an eddy rectifies onto an alternating spatial pattern of temperature advection with typical length-scale given by the eddy radius R.

In the presence of an ensemble of eddies following different trajectories, any associated mean advection depends on inhomogeneities in the magnitude of the large-scale gradients G_T and G_S, and thus on the presence of large-scale fronts. Preferred eddy trajectories or spatial variations in the number of eddies represent other possibilities. We observe that the expressions obtained do not depend on whether the eddies are cyclonic or anticyclonic (the sign of ε). A mixture of the two does ensure that the perturbation salinity and temperature fields, S' and T', vanish in the time mean. Perturbations to the mean field then arise through the second-order advective tendencies alone.

It is interesting to note from Eq. 9 that the temperature perturbation T' has the same distribution as the eddy height field E, and also the same sign if $G_T/fc > 0$. With $c < 0$, this suggests that eddies are more likely to maintain coherence against dissipation where the background temperature gradient is equatorward. Note however that the roles of T and S are symmetric in the present discussion, and we can consider eddies which propagate along isohalines by simply substituting S and S' with T and T', and vice versa, everywhere. The sign of both background and perturbation advection tendencies is then reversed.

The problem can in fact be generalised for an arbitrary eddy path and shape. The perturbation salinity and temperature fields are written

$$(\nabla_h S' \times \nabla_h T') = \nabla_h(\mathbf{U}_e \cdot \nabla_h S) \times \nabla_h(\mathbf{U}_e \cdot \nabla_h T), \tag{12}$$

where $\mathbf{U}_e = (1/f)\hat{\mathbf{z}} \times \nabla D$ and $D(x, y) := \int_{-\infty}^{t} E(x, y, t)\mathrm{d}t$. If we assume, as before, that on the spatial scales of interest $\nabla_h S$ and $\nabla_h T$ may be considered constant, then we obtain

$$\begin{aligned}(\nabla_h S' \times \nabla_h T') = {} & \\ & (\nabla_h S \times Z_e) \times (\nabla_h T \times Z_e) && \text{(I)}\\ & + (\nabla_h S \cdot \nabla)\mathbf{U}_e \times (\nabla_h T \times Z_e) \\ & \quad - (\nabla_h T \cdot \nabla)\mathbf{U}_e \times (\nabla_h S \times Z_e) && \text{(II)}\\ & + (\nabla_h S \cdot \nabla)\mathbf{U}_e \times (\nabla_h T \cdot \nabla)\mathbf{U}_e && \text{(III)}\end{aligned}$$

where we have defined $Z_e := \nabla \times \mathbf{U}_e$, the time-integrated vorticity. Terms (I) and (II) are proportional to Z_e^2, but they cancel each other out:

$$\text{(I)} = -\text{(II)} = (\nabla_h S \times \nabla_h T) Z_e^2.$$

Term (III) is equal to

$$\begin{aligned}(\nabla_h S' \times \nabla_h T') = \text{(III)} & \\ = -\frac{1}{4f^2}(\nabla_h S \times \nabla_h T) \cdot & \\ [4(\partial_x \partial_y D)^2 - 4(\partial_x^2 D)(\partial_y^2 D)]. & \end{aligned} \tag{13}$$

The expression in square brackets is formally identical with that for the Okubo–Weiss parameter Ξ of an eddy with a surface elevation field given by $D(x, y)$. For a stationary eddy, H and D are exactly proportional to each other, and the anomalous temperature advection generated by the eddy has the same pattern as $(-\xi)$, the O–W parameter of the eddy itself. We thus obtain a contribution to the mean advection of the same sign in the eddy core, and with the opposite sign at the edges. This is independent of the type of eddy considered. For a moving eddy whose amplitude does not change in time, the time-integrated height pattern D decays in the direction perpendicular to the eddy path but is constant along the path, except at the location of the eddy itself, where its shape is not yet averaged out. If the curvature of the path is small compared to the eddy's radius, Ξ is close to zero everywhere except at the location of the eddy. The crucial point is that along the path of the eddy core the localised contributions are all proportional to the negative of the O–W parameter and therefore they tend to have the same sign as the mean advection.

The main assumption we make is that the eddy maintains a coherent structure throughout and remains unaffected by the perturbation fields S' and T'. According to

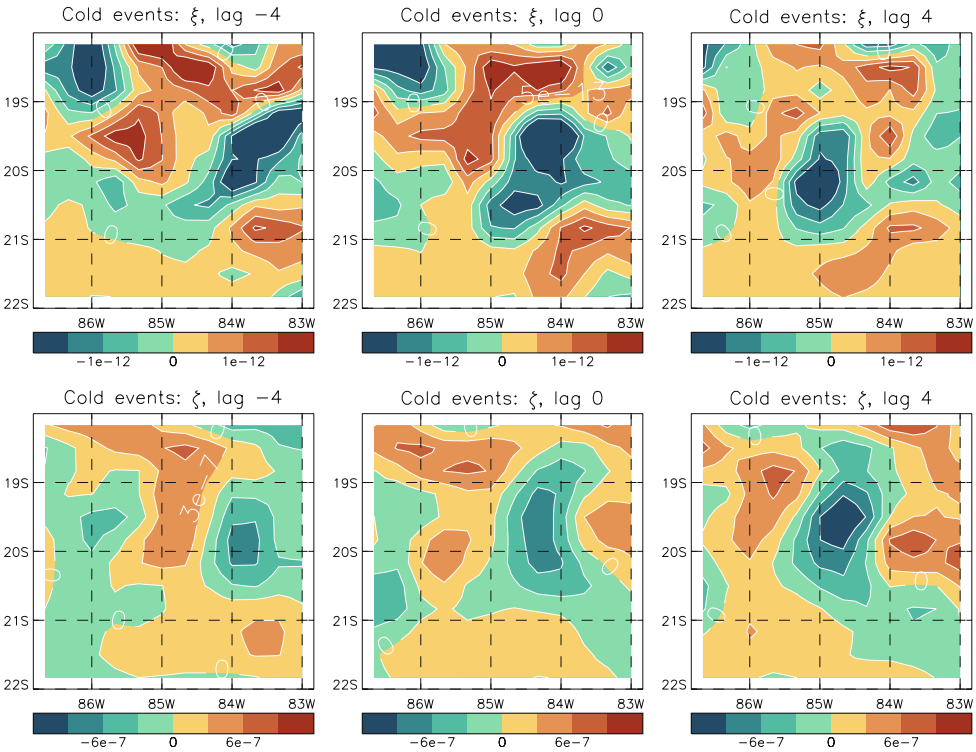

Fig. 16 Composites of the surface O–W parameter, ξ (*upper panels*), and vorticity, ζ (*lower panels*), for negative anomalies in the vertically-integrated temperature tendencies generated by geostrophic advection, from four pentads (20 days) before to 20 days after the peak. The apparent velocity of the eddy-like feature is approximately 3 cm/s

Eq. 9, in the case where the background salinity is homogeneous, or is aligned with the isotherms, this appears to be a justified assumption. The approximation will still hold if the eddy pressure field is determined by the thermal structure of the overlying water and is therefore largely unaffected by changes in T and S at the depth considered. Note that we do not consider here the temperature and salinity anomalies associated with the structure of the eddy itself, nor how they interact either with the mean flow or with the eddy advection field. This is a wider problem that exceeds the scopes of this paper, and that probably cannot be fully addressed with HiGEM.

Figure 16 supports the view that the cold advection events at 20S, 85W are associated with eddy-like structures as diagnosed by their vorticity (ζ) and the O–W parameter (ξ). In Fig. 16 the structure appears to move with a zonal speed consistent with that shown in Fig. 4; the ratio $|\zeta|/|\xi|$ is also similar. Indeed, the spatial association between the total "census" of O–W eddies, as defined in Sect. 2 (Fig. 4), with that of anomalous geostrophic advection, shown in Fig. 17, lends further support to the existence of a mechanistic link.

To summarise, we posit that the small-scale structure in the simulated advection field in the SEP is produced by some form of baroclinic eddy activity, controlled by large-scale fronts. Our tentative conceptual model helps in the interpretation of the main characteristics of transient advection: small spatial scale, "noisy" pattern organised along wider structures seemingly persisting in time, and

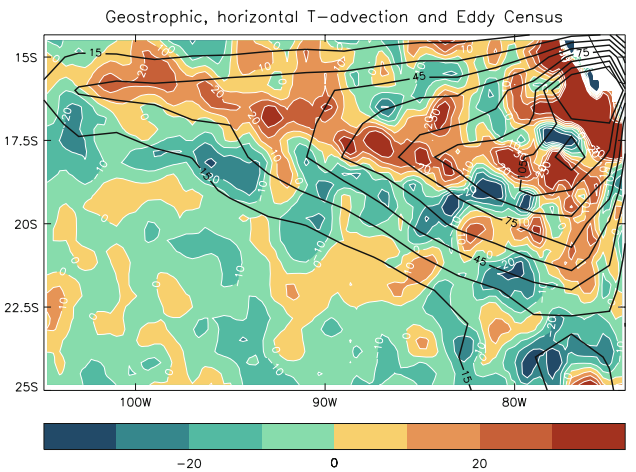

Fig. 17 Map of the vertically-integrated heat advection (in W/m^2) generated by geostrophic, horizontal advection (*colour coding*) and the number-density of O–W eddies, as defined in Sect. 2 (*black contours*) for 30 years of the HiGEM integration

apparent association with the strong salinity front related with the freshwater intrusion.

We note that residual advection patterns like those shown in Fig. 15 rely on either a very sharp frontal structure compared to its displacements, or spatial inhomogeneities in the occurrence of eddies, for example either because of generation sites or because of preferred propagation paths. In this latter case, the observed spatial scales for the rectifying pattern of advection is expected be bounded from below by the dominant eddy sizes, and from

above by the spatial scale characterising the eddy-number distribution. This is qualitatively consistent with Fig. 17.

Our conceptual model ignores the role of the vertical structure in the stratification, which is also affected by changes in the mixed layer, and ultimately by the surface forcing. Moreover, by the mechanisms discussed it is possible to generate a persistent pattern of cold and warm advection associated with transients, but with a vanishing or near-vanishing area average. Although this matches the model results to a first approximation, it is not rigorously satisfied from our data. Cold advection anomalies are preferentially associated with warm, fresh anomalies in the thermocline at 20S,85W. This points to further non-linearities of the system, possibly related with the subduction of surface anomalies. The surface SEP is characterised by a strong large-scale NW-ward surface salinity and temperature gradients. Anomalies in freshwater forcing, in this area can quickly generate anomalous $\nabla_h S \times \nabla_h T$ at the base of the mixed layer, thus potentially affecting the way in which the freshwater input is subducted.

In view of the climatological prevalence of evaporative fluxes in both heat and salinity surface budgets, precipitation anomalies may be particularly effective in locally altering the ocean's "spiciness" (water salinity at a constant-density surface). In this context, it is interesting to observe that the largest positive contribution to the heat advection tendencies from transients North of 17S is associated with the longer (interannual) time-scales (Fig. 12). These are more likely to be associated with cumulative surface forcing and the slow subduction of temperature and salinity anomalies in the seasonal cycle. In the sub-seasonal band, the residual long-term mean advection is also mostly positive and North of 17S, and in this case a connection with ENSO, specifically El-Niño events, is evident, with warming over the the NINO3.4 region followed by a warm pulse in the SEP, as may be expected from the excitation of fast, downwelling coastal Kelvin waves. (No equivalent relationship is apparent for La-Niña events). For both these components, advection variability is probably less strongly associated with free baroclinic eddies than for the inter-seasonal component, which shows no relationship with ENSO.

5 Discussion and conclusions

Oceanic heat advection in the south-eastern tropical Pacific simulated by the high-resolution global coupled general-circulation model HiGEM (1/3° × 1/3° in the ocean) locally gives significant long-term mean contributions to the heat budget of the water column.

At one particular location (20S, 85W) for which an observational estimate could be provided from the analysis of long time-series of in-situ oceanographic data (Colbo and Weller 2007), the simulated magnitude and sign of this effect matches that estimate. However, at nearby locations the model simulates contributions that are different both in magnitude and in sign.

To shed some light on the climate processes involved, we investigated the spatial and temporal characteristics of the structures associated with these rectifying advective anomalies and attempted a physical interpretation for their generation. Either spatially or temporally, both advection by the mean field and mean advection from transients are highly variable. The latter item, in particular, is dominated by small length scales (200–450 km) and long time-scales (>4 months). The relevant activity appears to be preferentially located at the depth of the oceanic thermocline. Qualitatively, these results are in good agreement with the high-resolution regional simulations of Capet et al. (2008, 2009, in preparaion).

The evidence we find suggests that at least part of such transient advection is dependent on the existence of a fresh intrusion from higher latitudes along the east-Pacific seaboard. The currents associated with large, non-linear baroclinic eddies can cause local deformations of the front and thus generate rectifying anomalous temperature and salinity advection. Such interpretation implies that a thickness-diffusion parametrisation of the Gent–McWilliams type (Gent et al. 1995) may not capture—in models with lower resolution—advection transients like those described here. In addition to the limited ability to represent steep slopes of the thermocline on a grid spacing with $\Delta z/\Delta x \sim 10^{-5}$, due to the strong salinity-temperature compensation in the SEP, the thickness-gradient anomalies are generally much smaller. Moreover, they tend to be aligned with isotherms (Fig. 13), resulting in vanishing temperature advection by the Gent–McWilliams velocities.

The "noisy" spatial pattern in particular supports the view that the ability of the model to resolve the dynamical features associated with advection transients (i.e., according to our interpretation, sharp fronts and baroclinic waves in the pycnocline) critically depends on its resolution. The characteristics of mesoscale features and their relation with the mean flow may depend on the smallest resolved scale, and affect the mean effect of such structures up to scale comparable to the synoptic scales of the atmosphere, with impacts on the atmosphere–ocean coupling. With regard to this, a comparison with the lower-resolution version of the model, HadGEM, is shown in Fig. 18, when the advection fields of both represented on the coarser grid-size. This highlights the large-scale dipolar structure of the rectifying transient in the high-resolution integration which is not present in HadGEM. Thus, even if when averaged over regional scales the power spectrum of the column

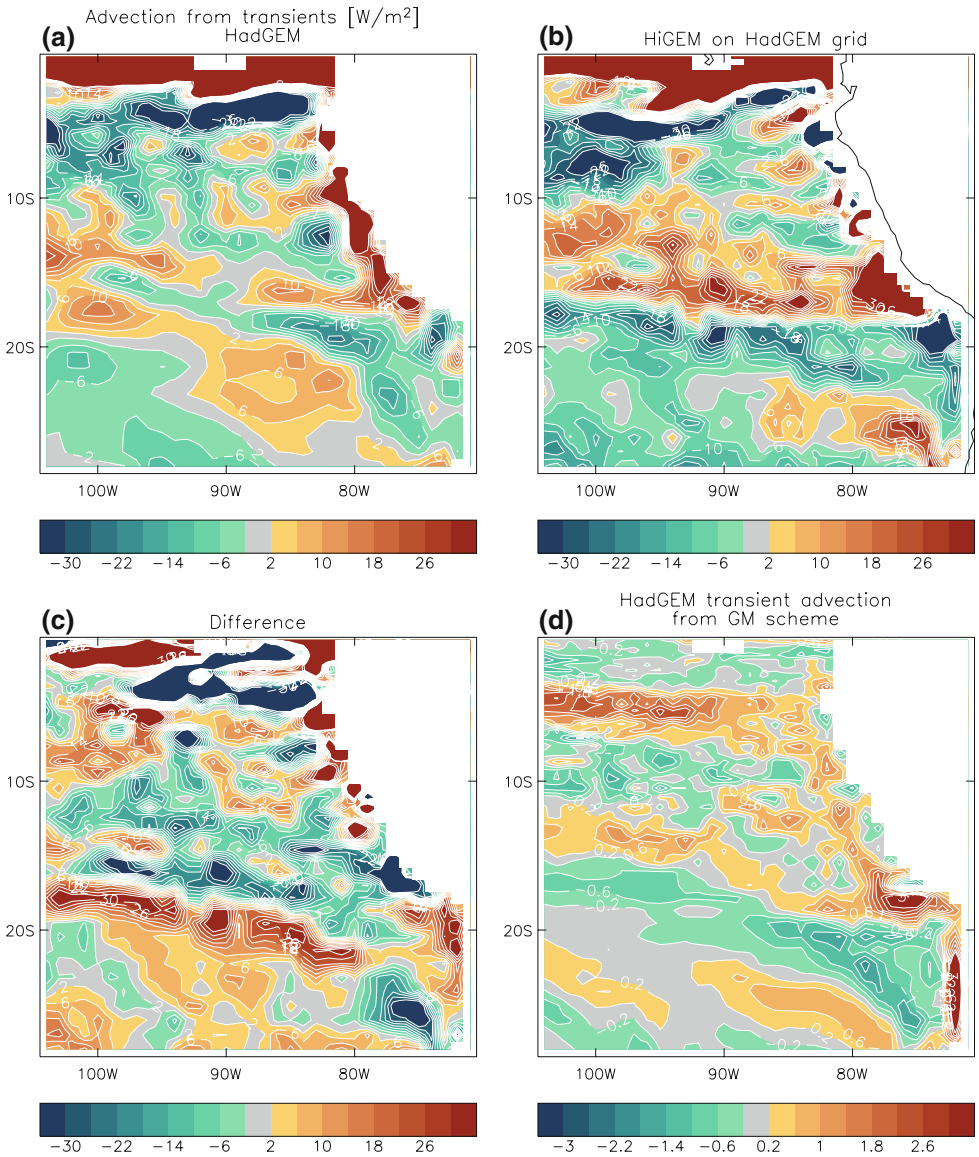

Fig. 18 Maps of oceanic heat-advection tendency, in W/m^2, from transients: **a** for the lower-resolution model, HadGEM; **b** for the higher-resolution model, HiGEM, averaged over HadGEM grid-boxes. **c** Difference plot of **a** and **b**. **d)** Heat advection in HadGEM originating from the transient component of Gent–McWilliams fluxes

integrated advection are very similar in the two integrations (not shown), the rectifying components, and therefore those responsible for the maintenance of the oceanic heat budget, differ considerably. We also show in Fig. 18 that the contribution from the Gent–McWilliams parametrisation (Gent et al. 1995) in the HadGEM integration. This contribution to the advection can be written as $-u^*\nabla T$ with $u^* = -\kappa\partial_z(\nabla_h\rho/\partial_z\rho)$, and $\kappa = 150$ m^2/s in HadGEM. It generally tends to correct the low-resolution ocean model towards a better agreement with the high-resolution simulation. However, its magnitude is too small, with values less than 2 W/m^2 against differences (and HiGEM eddy-advection tendencies) of $\sim$20 W/m^2. Compared to either the difference pattern in panel (c) of Fig. 18 or with the HiGEM eddy patterns seen in Figs. 6, 7, and 10, advection generated by Gent–McWilliams fluxes tends to be too strongly confined near the coastal area.

The peculiar spatial pattern of the transient ocean heat advection found in our analysis implies that eddy advection tendencies can be both positive and negative, and change sign between geographically close locations. Over the larger SEP area (100W–75W, 25S–10S), the average mean eddy advection from HiGEM is small and positive (2.4 W/m^2), thus contributing, on the larger area and in the long-term mean, to warm the ocean rather than to cool it.

Most of this residual is associated with interannual anomalies, with a significant "fast" contribution from El-Niño events. The advection mean associated with anomalies on the inter-seasonal time-scales (4–12 months), which are those most likely associated with eddies and the mechanisms described in this paper, remains negative (-0.5 W/m^2). Be that as it may, Figs. 7 and 12 indicate that this component alone, even when limited to geostrophic advection, is positive in certain areas, mainly

North of 17S. This is partly determined by the mean advection field which is spatially "noisy" itself and does not compensate the smooth spatial distribution of surface heat fluxes. Moreover, as demonstrated in Fig. 9, eddy advection tendencies in the same location can change markedly from one year to the other, with no short-term (i.e. annual) closure of the heat budget.

To conclude, in the light of our findings the agreement between the model-simulated advection at 20S, 85W and the estimate of Colbo and Weller (2007) appears somewhat fortuitous. First, a slight change in location of the buoy would have led to a different assessment of the model's simulation. Second, at the two grid-points next to 20S, 85W, transient temperature advection in the model leaves typical unbalanced heat tendencies of the order of 10 W/m^2 over periods of four years, thus adding a further uncertainty to the estimate of Colbo and Weller (2007) which is based on a closed heat budget. It might be the case that the fluctuating property of the mean oceanic advection field is not realistic, implying smaller uncertainties for Colbo and Weller's (2007) estimate, but also invalidating the model anyway. On the other hand, it might be that Colbo and Weller's (2007) estimation method for Ekman and geostrophic advection, which in part makes use of World Ocean Atlas' data, implicitly accounts for slow variability. These are hypotheses that need to be observationally tested, since it might well be that the heat budget on a particular location is not, in general, representative for the larger area. Such a conclusion would have far-reaching implications for the observational strategies that need to be adopted for such estimates.

From a modelling viewpoint, even if the limitations of the observational framework make it difficult to quantify possible errors, our results indicate that at 1/3° resolution coupled climate models are, in principle, capable of producing a level of small-scale heat-budget variability comparable to observational estimates. This important result, combined with the contrast between HiGEM and the lower-resolution ($\sim 1° \times 1°$) HadGEM model, highlights the importance of carrying out a comparison with truly eddy-resolving integrations, such as those of Capet et al. (2009, in preparaion), in order both to understand if, or how closely, numerical convergence is achieved, and to assess the robustness of the oceanic mechanisms for variability described here.

Acknowledgments We are grateful to John Donners, Robert Weller, Jim McWilliams, and Remi Tailleux for stimulating discussions. We wish to thank Ian Stevens and Dudley Chelton for constructive comments and suggestions to the manuscript. We also thank Ken Takahashi and an anonymous reviewer for helpful comments. This work was supported by the UK National Centre for Atmospheric Sciences (NCAS-Climate).

References

Bony S, Dufresne J-L (2005) Marine boundary layer clouds at the heart of tropical cloud feedback uncertainties in climate models. Geophys Res Lett 32:L20806. doi:10.1029/2005GL023851

Capet X, Colas F, Penven P, Marchesiello P, McWilliams JC (2008) Eddies in Eastern-boundary subtropical upwelling systems. In: Hecht MW, Hasumi HH (eds) Ocean modeling in an Eddying regime, Geophysical monograph series, vol 177. AGU, Washington DC, 350 pp

Chaigneau A, Gizolme A, Grados C (2008) Mesoscale eddies off Peru in altimeter records: identification algorithms and eddy spatio-temporal patterns. Prog Oceanography 79:106–119

Chelton DB, Schlax MG, Samelson RM, de Szoeke RA (2007) Global observations of large oceanic eddies. Geophys Res Lett 34:L15606

Colbo K, Weller RA (2007) The variability and heat budget of the upper ocean under the Chile-Peru stratus. J Mar Res 65:607–637. doi:10.1357/002224007783649510

Conkright ME, Locarnini RA, Garcia HE, O'Brien TD, Boyer TP, Stephen C, Antonov JI (2002) World Ocean Atlas 2001: objective analyses, data statistics, and figures. CD-ROM Documentation, National Oceanographic Data Center, Silver Spring, MD, 17 pp

Cronin MF, Bond NA, Fairall CW, Weller RA (2006) Surface cloud forcing in the east Pacific Stratus Deck/Cold Tongue/ITCZ complex. J Clim 19:392

Davies T, Cullen MJP, Malcolm AJ, Mawson MH, Staniforth A, White AA, Wood N (2005) A new dynamical core for the Met Office's global and regional modelling of the atmosphere. Q J R Meteorol Soc 131:1759–1782

de Szoeke SP, Xie S-P (2007) The tropical eastern Pacific seasonal cycle: assessment of errors and mechanisms in IPCC AR4 coupled ocean-atmosphere general circulation models. J Clim 21:2573–2590

Dukowicz JK, Smith RD (1994) Implicit free surface method for the Bryan-Cox-Semtner ocean model. J Geophys Res 99:7991–8014

Gent PR, Willebrand J, McDougall TJ, McWilliams JC (1995) Parameterizing eddy-induced tracer transports in ocean circulation models. J Phys Oceanogr 25:464

Griffies SM, Gnanadesikan A, Pacanowski RC, Larichev VD, Dukowicz JK, Smith RD (1998) Isoneutral diffusion in a z-coordinate ocean model. J Phys Oceanogr 28:805–830

Hastenrath S (1991) Climate dynamics of the tropics. Kluwer, Dordrecht, pp 156–158

IPCC (2007) Climate change 2007: the physical science basis. In: Solomon S, Qin D, Manning M, Chen Z, Marquis M, Averyt KB, Tignor M, Miller HL (eds) Contribution of Working Group I to the fourth assessment report of the Intergovernmental Panel on climate change. Cambridge University Press, Cambridge, 996 pp

Johns TC et al (2006) The New Hadley Centre Climate Model (HadGEM1): evaluation of coupled simulations. J Clim 19:1327–1353

Klein P (2008) High-frequency winds and eddy-resolving models (in preparation)

Kraus EB, Turner JS (1967) A one-dimensional model of the seasonal thermocline. Tellus 19:98–105

Large WG, Danabasoglu G, Doney SC, McWilliams JC (1997) Sensitivity to surface forcing and boundary layer mixing in a global ocean model: annual-mean climatology. J Phys Oceanogr 27:2418–2447

Lock AP, Brown AR, Bush MR, Martin GM, Smith RNB (2000) A new boundary layer mixing scheme. Part I: scheme description and SCM tests. Mon Weather Rev 128:3187–3199

Ma C-C, Mechoso CR, Robertson AW, Arakawa A (1996) J Clim 9:1635

Manganello JV, Huang B (2008) The influence of systematic errors in the southeast pacific on ENSO variability and prediction in a coupled GCM. Clim Dyn. doi:10.1007/s00382-008-0407-5

Martin GM, Ringer MA, Pope VD, Jones A, Dearden C, HintonTJ (2006) The physical properties of the atmosphere in the New Hadley Centre Global Environmental Model (HadGEM1). Part I: model description and global climatology. J Clim 19:1274–1301

McDougall TJ, Jackett DR, Wright DG, Feistel R (2003) Accurate and computationally efficient algorithms for potential temperature and density of seawater. J Atmos Ocean Technol 20:730–741

Mechoso CR, Robertson AW, Barth N, Davey MK, Delecluse P, Gent PR, Ineson S, Kirtman B, Latif M, Le Treut H, Nagai T, Neelin JD, Philander SGH, Polcher J, Schopf PS, Stockdale T, Suarez MJ, Terray L, Thual O, Tribbia JJ (1995) The seasonal cycle over the tropical Pacific in coupled ocean-atmosphere general circulation models. Mon Weather Rev 123:2825

Mitchell TP, Wallace JM (1992) The annual cycle in equatorial convection and sea surface temperature. J Clim 5:1140

Norris JR, Leovy CB (1994) Interannual variability in stratiform cloudiness and sea surface temperature. J Clim 7:1915

Pacanowski RC, Griffies SM (1998) MOM3.0 manual. NOAA/GFDL, Princeton, 692 pp

Penven P, Echevin V, Pasapera J, Colas F, Tam J (2005) Average circulation, seasonal cycle, and mesoscale dynamics of the Peru current system: a modelling approach. J Geophys Res 110:C10021. doi:10.1029/2005JC002945

Philander SGH, Gu D, Lambert G, Li T, Halpern D, Lau N-C, Pacanowski RC (1996) Why the ITCZ is mostly north of the equator. J Clim 9:2958

Rahmstorf S (1993) A fast and complete convection scheme for ocean models. Ocean Model 101:9–11

Reynolds RW, Smith TM, Liu C, Chelton DB, Casey KS, Schlax MG (2007) Daily high-resolution blended analyses for sea surface temperature. J Clim 20:5473–5496

Ringer MA, Martin GM, Greeves CZ, Hinton TJ, James PM, Pope VD, Scaife AA, Stratton RA, Inness PM, Slingo JM, Yang G-Y (2006) The physical properties of the atmosphere in the New Hadley Centre Global Environmental Model (HadGEM1). Part II: aspects of variability and regional climate. J Clim 19:1302–1326

Roberts MJ, Marshall D (1998) Do we require adiabatic dissipation schemes in eddy-resolving ocean models?. J Phys Oceanogr 28:2050–2063

Roberts MJ, Clayton A, Demory M-E, Donners J, Vidale PL, Norton WA, Shaffrey LC, Stevens I, Stevens DP, Wood RA, Slingo J (2009) Impact of resolution on the tropical Pacific circulation in a matrix of coupled models. J Clim (submitted)

Schlax MG, Chelton DB (1992) Frequency domain diagnostics for linear smoothers. J Amer Stat Assoc 87:1070–1081

Shaffrey L, Stevens I, Warwick N, Roberts M, Vidale P-L, Harle J, Jrrar A, Stevens D, Woodage M, Demory M-E, Donners J, Clark D, Clayton A, Cole J, Wilson S, Connolley W, Davies T, Iwi A, Johns T, King J, New A, Slingo JM, Slingo A, Steenman-Clark L, Martin G (2009) UK-HiGEM: the new high-resolution global environmental model. Model description and evaluation. J Clim. doi:10.1175/2008JCLI2508

Stevens DP et al (2009) UK-HiGEM: the new UK high resolution global environment model. Ocean spin-up and evaluation. Ocean Sci (to be submitted)

Takahashi K, Battisti DS (2007) Processes controlling the mean tropical Pacific precipitation pattern. Part I: the Andes and the easter Pacific ITCZ. J Clim 20:3434–3451

Toniazzo T (2009) Climate variability in the south-eastern Pacific and its relation with ENSO: a GCM study. Clim Dyn. doi:10.1007/s00382-009-0602-z

Uppala SM et al (2005) The ERA-40 re-analysis. Q J R Meteorol Soc 131:2961–3012

Yu J-Y, Mechoso CR (1999) A discussion on the errors in the surface heat fluxes simulated by a coupled GCM. J Clim 12:416–426